# STRUCTURAL AND AERODYNAMIC INTERACTION COMPUTATIONAL TOOL FOR HIGHLY RECONFIGURABLE WINGS

A Thesis

by

BRIAN JOSEPH EISENBEIS

Submitted to the Office of Graduate Studies of
Texas A&M University
in partial fulfillment of the requirements for the degree of

MASTER OF SCIENCE

August 2010

Major Subject: Aerospace Engineering

# STRUCTURAL AND AERODYNAMIC INTERACTION COMPUTATIONAL TOOL FOR HIGHLY RECONFIGURABLE WINGS

A Thesis

by

BRIAN JOSEPH EISENBEIS

Submitted to the Office of Graduate Studies of
Texas A&M University
in partial fulfillment of the requirements for the degree of

MASTER OF SCIENCE

Approved by:

| | |
|---|---|
| Chair of Committee, | John Valasek |
| Committee Members, | Walter E. Haisler |
| | John E. Hurtado |
| | Jose Roesset |
| | Thomas W. Strganac |
| Head of Department, | Dimitris Lagoudas |

August 2010

Major Subject: Aerospace Engineering

# ABSTRACT

Structural and Aerodynamic Interaction
Computational Tool for Highly Reconfigurable Wings. (August 2010)
Brian Joseph Eisenbeis, B.S., Texas A&M University
Chair of Advisory Committee: Dr. John Valasek

Morphing air vehicles enable more efficient and capable multi-role aircraft by adapting their shape to reach an ideal configuration in an ever-changing environment. Morphing capability is envisioned to have a profound impact on the future of the aerospace industry, and a reconfigurable wing is a significant element of a morphing aircraft. This thesis develops two tools for analyzing wing configurations with multiple geometric degrees-of-freedom: the structural tool and the aerodynamic and structural interaction tool. Linear Space Frame Finite Element Analysis with Euler-Bernoulli beam theory is used to develop the structural analysis morphing tool for modeling a given wing structure with variable geometric parameters including wing span, aspect ratio, sweep angle, dihedral angle, chord length, thickness, incidence angle, and twist angle. The structural tool is validated with linear Euler-Bernoulli beam models using a commercial finite element software program, and the tool is shown to match within 1% compared to all test cases. The verification of the structural tool uses linear and nonlinear Timoshenko beam models, 3D brick element wing models at various sweep angles, and a complex wing structural model of an existing aircraft. The beam model verification demonstrated the tool matches the Timoshenko models within 3%, but the comparisons to complex wing models show the limitations of modeling a wing structure using beam elements. The aerodynamic and structural interaction tool is developed to integrate a constant strength source doublet panel method aerodynamic tool, developed externally to this work, with the

structural tool. The load results provided by the aerodynamic tool are used as inputs to the structural tool, giving a quasi-static aeroelastically deflected wing shape. An iterative version of the interaction tool uses the deflected wing shape results from the structural tool as new inputs for the aerodynamic tool in order to investigate the geometric convergence of an aeroelastically deflected wing shape. The findings presented in this thesis show that geometric convergence of the deflected wing shape is not attained using the chosen iterative method, but other potential methods are proposed for future work. The tools presented in the thesis are capable of modeling a wide range of wing configurations, and they may ultimately be utilized by Machine Learning algorithms to learn the ideal wing configuration for given flight conditions and develop control laws for a flyable morphing air vehicle.

To my parents and sister: Kathy, Kevin, and Laura, for their unwavering support and love

# ACKNOWLEDGMENTS

I would like to thank the American Society for Engineering Education for the National Defense Science and Engineering Graduate Fellowship which provided personal financial support and enabled me to pursue graduate studies. I would also like to thank Dr. John Valasek for his mentorship and countless hours of support over the past few years, as well as Dr. Walter Haisler, Dr. John Hurtado, Dr. Jose Roesset, Dr. Thomas Strganac, the Vehicle Systems and Control Laboratory at Texas A&M University, and my family and friends for all of their support throughout my graduate studies.

This work was sponsored (in part) by the Air Force Office of Scientific Research, USAF, under grant/contract number FA9550-08-1-0038. The technical monitor was Dr. William M. McEneaney. The views and conclusions contained herein are those of the author and should not be interpreted as necessarily representing the official policies or endorsements, either expressed or implied, of the Air Force Office of Scientific Research or the U.S. Government.

TABLE OF CONTENTS

CHAPTER Page

# LIST OF TABLES

# LIST OF FIGURES

FIGURE Page

FIGURE Page

# CHAPTER I

# INTRODUCTION

This chapter states the engineering problem which will be addressed by the research and identifies the significance and impact that a reconfigurable wing may have on the aerospace engineering field. This chapter will also discuss some of the history of the morphing wing problem and will highlight key literature addressing this research issue. Finally, the chapter will describe the research issues, objectives, scope, and methods.

## A. Problem Identification and Significance

When the Wright Brothers first flew in 1903, their plane had flexible wings which were warped during flight for better control. As planes began to fly at faster speeds, it became necessary to use structurally stiff wings to accommodate higher wing loading. In different flight regimes, there is an optimum wing shape that provides the best performance for the given flight conditions. Morphing, which is the changing from one geometrical shape to another, can be used to improve the aerodynamic performance of an aircraft wing in different flight regimes.

A morphing air vehicle will have an immense impact on the aerospace industry. In modern society, efficiency is critical and this new technology could allow planes to be more fuel efficient. Morphing technology will give each plane a wider range of roles or possible mission objectives and allow the aircraft to be more versatile. The military currently has certain aircraft that are used for specific tasks such as speed, range, or maneuverability. One morphing aircraft could possibly fulfill various roles

---

The journal model is *IEEE Transactions on Automatic Control.*

by changing its geometry. Using only one plane for numerous types of missions would save money and be more effective.

There are many parameters of a wing that can be effectively morphed to impact the flight of the aircraft. Parameters defining the cross-sectional airfoil may also be morphed to improve the wing performance. Parameters defining the wing and airfoil include the following:

- $b$ Wing span
- $S$ Wing area
- $\Lambda$ Sweep angle
- $\Gamma$ Dihedral angle
- $\alpha_r$ Root incidence angle
- $\alpha_t$ Tip incidence angle
- $c_r$ Root chord length
- $c_t$ Tip chord length
- $t_r$ Root thickness
- $t_t$ Tip thickness

Other airfoil properties may also be used for morphing but will not be addressed in the research. Figure 1 below shows various parameters of a wing. Figure 2 shows several airfoil parameters which may be effectively morphed.

There are numerous challenges associated with the development of a morphing air vehicle. The actuation mechanics provide a significant challenge, especially when

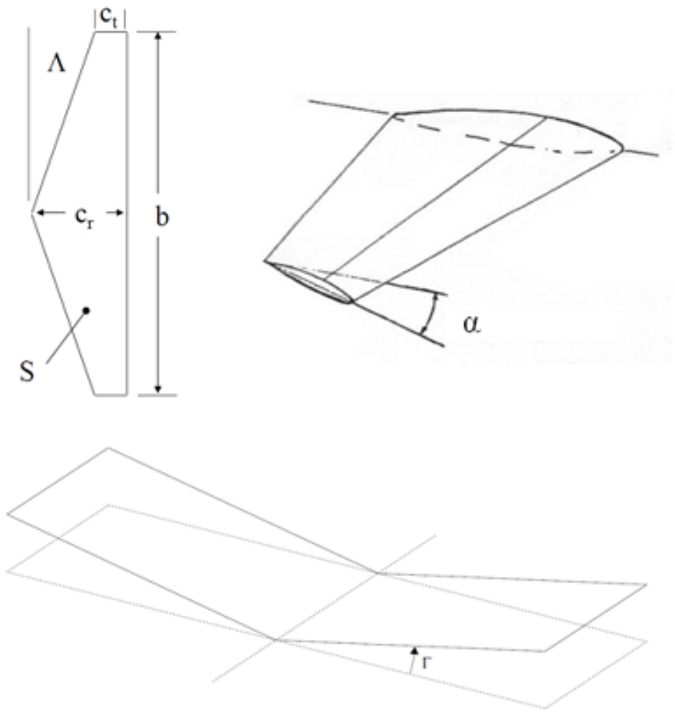


Fig. 1. Wing Geometry and Nomenclature

multiple degrees of freedom are utilized for morphing. Multiple actuators must be controlled quickly and simultaneously, and it may be necessary to locate these actuators throughout the entire wing. Materials also provide a challenge because the wing must be structurally stiff but capable of changing shape. Many morphing air vehicles use smart materials to allow for large shape changes. Also, deciding which morphed geometry is best suited for the current flight condition is another difficulty of morphing. To make a decision regarding the wing and airfoil parameter values, a strong understanding of the current aerodynamic and structural implications is needed. With multiple wing and airfoil morphing parameters, an infinite number of morphed wing configurations are possible. Because it is necessary to have aerody-

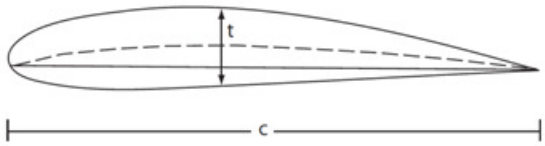


Fig. 2. Airfoil Geometry and Nomenclature

namic and structural knowledge for all of these cases, robust and accurate aerodynamic and structural tools are needed to determine the wing shape which provides the best aerodynamic and aeroelastic characteristics while maintaining the structural integrity of the wing. Aeroelasticity is the relationship between the aerodynamic loads and structural deformations, and the primary parameters of interest include the lift, aerodynamic pitching moment, displacements, and rotations. All of the previously mentioned challenges must be addressed in order to effectively fly and control a morphing air vehicle.

The research will take a general approach and consider a hypothetical morphing wing which can have large geometric changes in various wing and airfoil parameters. The goal is to develop the methods needed to analyze the structural and aerodynamic effects of the general morphing wing and create an analysis and simulation tool. By developing computational tools for a general morphing wing, the same analysis tools can be used for multiple aircraft which have different morphing capabilities.

It will be necessary to utilize a structural analysis tool and an aerodynamic analysis tool. The structural analysis tool will use Finite Element Analysis (FEA) and work in conjunction with an existing Computation Fluid Dynamics Doublet Panel Method tool used to model and simulate aerodynamic effects on a morphing wing [1], [2]. The aerodynamic forces provided by the aerodynamic tool will be used by

the structural tool to determine the deflected wing geometry as well as the axial stresses within the wing. By iterating between the aerodynamic and structural tools, a converged solution for the deflected wing geometry may be obtained, providing insight to the quasi-static aeroelastic wing properties.

The ultimate use of the method and tool is to work within a framework which utilizes various Machine Learning tools that can analyze the aerodynamic and structural data for a wing at a given flight condition to determine the configuration for optimal wing geometry [3], [4], [5]. The structural tool will generate the deflections and stresses based on the input aerodynamic loads and the wing configuration. The deflection and stress values will be passed to the Machine Learning algorithms for numerous morphing cases at various flight conditions, so realistic deformations and stresses are utilized. If stresses exceed the material limitations, the Machine Learning algorithm will determine a different shape or flight condition in order to maintain the structural integrity [6], [7].

## B. Literature Review

The general focus of the research is on reconfigurable air vehicles, and the specific area of focus is on the structure of reconfigurable systems.

### 1. Reconfigurable Air Vehicles

In the past, planes such as the Grumman F-14 and the North American Rockwell B-1 have used mechanical actuation to employ variably swept wings, allowing for better performance during supersonic flight. These planes are shown in Figure 3.

Since the F-14 and B-1, considerable advancements have been accomplished in the field of morphing air vehicles. Many of the recent studies of morphing aircraft have

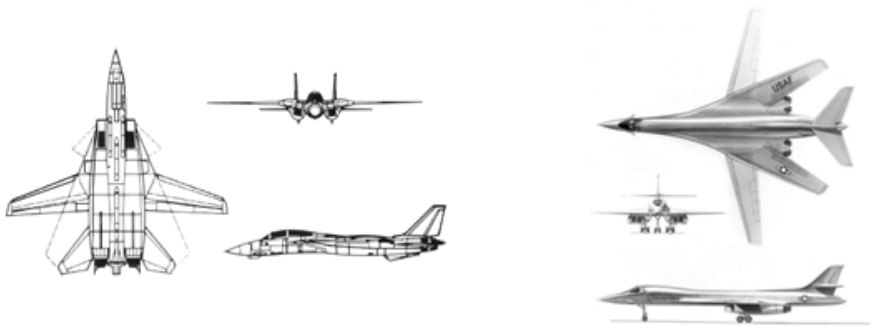

Fig. 3. Grumman F-14 (left) and North American Rockwell B-1 (right)

been inspired by nature. A group at Cornell University has analyzed various birds and their wing shapes at different speeds. Instincts help the birds find the optimal shape for morphing their wings [8]. Figure 4, taken from Wickensheiser, shows the various wing shapes for a hawk and a pigeon at different speeds. This reference along with Reference [9] discuss the aerodynamic performance and dynamic impacts due to morphing.

Others, such as the University of Florida, have also looked to nature for morphing in flight. Florida University has developed a flapping type model which is shown in Figure 5 [10]. In Reference [11], Motamed and Yan discuss the use of a flapping wing for an insect size micro aerial vehicle (MAV). This reference describes the implementation of a reinforcement learning algorithm on a dynamically scaled unsteady aerodynamic model at low Reynolds numbers. The experimental results show that the reinforcement learning method is valid for the MAV control problem. Reference [12] describes the use of an aerodynamic shape optimization program to obtain the optimal airfoil shape for a given flight condition of a light unmanned air vehicle. The program is based on a computational fluid dynamics solver with the Spalart-Allmaras

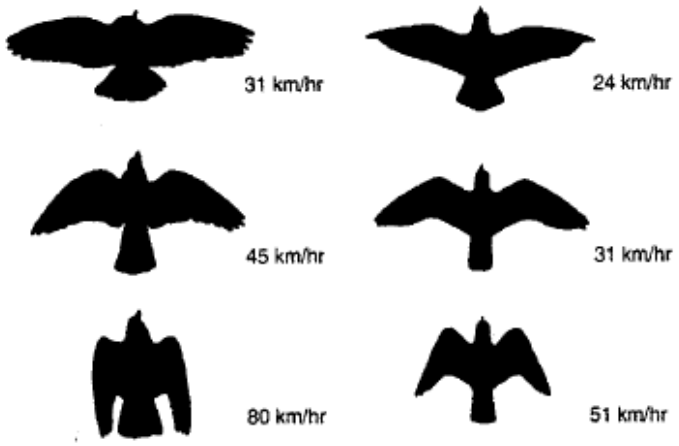


Fig. 4. Wing Morphologies for Hawks (Left) and Pigeons (Right) [8]

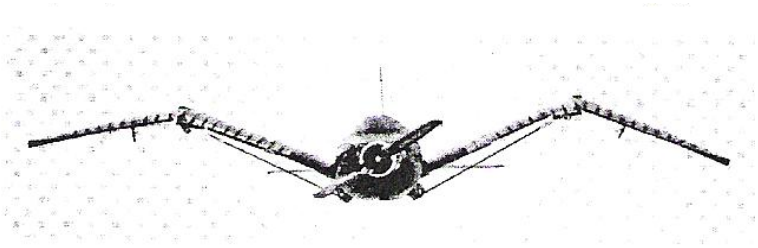

Fig. 5. Variable Gull-Wing Morphing Aircraft Model [10]

turbulence model and a sequential-quadratic-programming algorithm.

The United States Defense Advanced Research Projects Agency (DARPA) and Northrop Grumman, completed extensive testing on their morphing program called Smart Wing. This program developed a hingeless, smart-materials-based, control surface and wind tunnel tested it in two phases. Phase 1 tested the technology on a half span F-18 wing and Phase 2 tested it on a full-span unmanned combat air vehicle. Shape Memory Alloy (SMA) torque tubes and piezoelectric motors were used in dif-

ferent tests to actuate the morphing. The wind tunnel studies by Northrop Grumman have demonstrated improvements in lift, roll moment, and pitching moment making the aircraft more efficient and more controllable [13]. Testing also showed significant improvements in the pressure distribution over a smart morphing wing test article by delaying the flow separation at the trailing edge [14].

Morphing technology will give each plane a wider range of roles or possible mission objectives as demonstrated by the NextGen Morphing Aircraft Structures (N-MAS) Program. This study and wind tunnel test completed by DARPA, the Air Force Research Laboratory (AFRL), and NextGen Aeronautics concluded that morphing aircraft are very beneficial for a mission with hunter-killer parameters. For this mission type, morphing aircraft could theoretically reduce the sortie rate by 30% for vehicles less than 20,000 lbs which means fewer aircraft would be needed. This same study also compared the performance of a morphing vehicle versus a fixed wing aircraft as shown in Figure 6 below [15]. As shown in Figure 6, the morphing aircraft

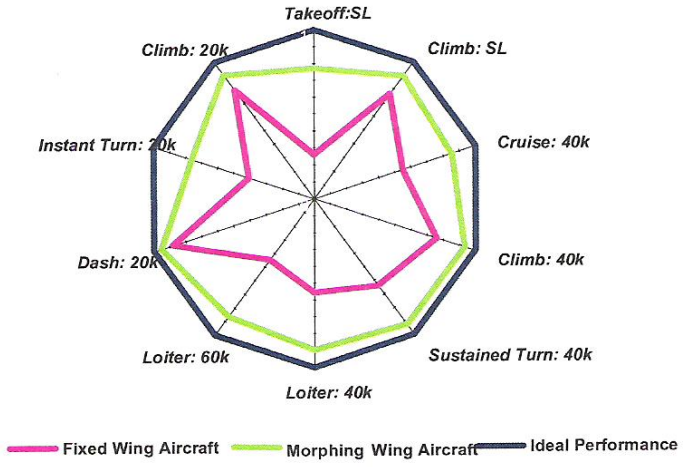


Fig. 6. Spider Plot Comparison of Fixed and Morphing Wing Aircraft [15]

is far superior to the fixed wing aircraft in every performance category. A picture of the N-MAS wind tunnel test is shown in Figure 7.

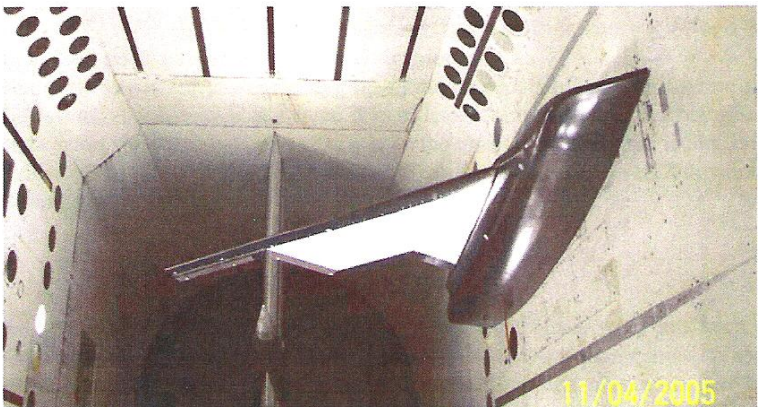


Fig. 7. Batwing Model in the NASA Langley TDT Wind Tunnel [15]

## 2. Structure of Reconfigurable Systems

Reference [16] discussed the aerodynamic and structural impacts of variable-span morphing used on a cruise missile. A subsonic doublet-hybrid method panel code was used to analyze the aerodynamics. It showed that increasing the wingspan improved the aerodynamic properties by increasing the lift while reducing the drag, leading to an increased range. Anti-symmetric span changes led to improved roll control. The structural and aeroelastic characteristics of the variable-span wing were investigated using an MSC/NASTRAN model of the wing-box structure. The model used two wings sections with the extendable wing section constrained to the main wing. Analysis showed that when the span increased, the torque at the wing root decreased considerably and increased at the wing tip slightly, so a variable-span morphing wing does not require a larger wing torsional stiffness. Results also showed that the bending moment for the extended wing increased dramatically, requiring a

need for an increased bending stiffness. Static aeroelastic analysis showed that the wing tip deformations increased with an increase in span, and the divergence boundary considerably decreased so the extended wing experienced divergence at a lower dynamic pressure.

Reference [17] describes and validates the structural and aerodynamic tools used for the static aeroelastic analysis of a morphing wing. Equivalent plate continuum models for the structure were utilized rather than a discrete finite element approach, and the aerodynamic loads were provided by an incompressible, quasi-steady vortex lattice code. Three equivalent plate methods were discussed: Classical Plate Theory (CPT), First-order Shear Deformation Theory (FSDT), and Higher-order Shear Deformation Theory (HSDT). A wing box was modeled using CPT and FSDT, and the mass and stiffness matrices for the spars, spar caps, ribs, rib caps, and skin were combined to obtain the wing mass and stiffness matrices. The CPT and FSDT models were validated using a NASTRAN finite element model, and FSDT proved to be more accurate. Because the aerodynamic loads depend upon the structural deflections, a feedback-loop between the aerodynamics and structure was necessary. A preliminary case showed aerodynamic coefficient and vertical displacement results at varying sweep angles.

In Reference [18], Nguyen develops the governing structural dynamic equations of motion for a flexible wing and accounts for the coupling of the aeroelasticity of flexible airframe components, the inertial forces due to rigid-body accelerations, and the propulsive forces. Wing bending and twist degrees of freedom are included in the structural dynamics equations. A finite-element method was used to solve for the aeroelastic deflections. The analysis assumes for high aspect ratio wings the equivalent beam approach with equivalent stiffness properties accurately captures the elastic behavior and structural deflections of the wing.

Many groups have conducted research on the technology needed for the structure of a morphing vehicle. Reference [19] discusses the use of an actuation system to accomplish spanwise curvature that allows for near-continuous bending of a wing. The two actuation systems described and tested were a tendon-based DC motor actuated system and a SMA-based mechanism. Reference [20] discusses the internal structure of the same spanwise bending wing. This reference also discusses the need for a compliant skin which would cover the wing joints and allow for in-plane stretching of the skin, while maintaining flexural rigidity.

Reference [21] describes various types of smart materials used for morphing actuation. It specifically describes the adaptive structures used in the Smart Wing program, and it discusses various adaptive control surfaces and SMA based actuation systems. Reference [22] shows the importance of shape estimation for deforming structures, and it investigates three types of shape sensing systems. Reference [23] explored the use of a dynamic shape control system for a morphing airfoil which consisted of two beams pinned at either end. The results showed that the actuation and control systems successfully and accurately commanded the airfoil shape.

## C. Research Issues

This section discusses some of the issues that will be addressed in the research. As stated in Section I, the primary research objective will be to develop a Finite Element Analysis tool which can be used for analysis of a morphing wing. To successfully and accurately achieve the overall research goal, several key research issues must be addressed.

### 1. Selection of Structural Analysis Method

Various types of elements may be used for Finite Element Analysis including Euler-Bernoulli beam elements, shell elements, and brick elements. Beam elements are used to approximate long, slender members; shell elements are used to approximate thin surfaces; brick elements are used to approximate three dimensional objects. Because brick and shell elements are more computationally intensive, beam elements are the most reasonable method provided the wing is relatively long and slender. [24], [25] Because the thickness of the wing is much smaller than the span, beam elements are feasible if the chord length is small compared to the span which is the case for a normal to high aspect ratio wing.

Linear or nonlinear analysis may be used in Finite Element Analysis. The research will pursue a linear method to simplify the computations. Linear analysis is very accurate when the deformations are relatively small when compared to the size of the overall structure and when there are not large torsional effects present.

### 2. Beam Theory Limitations and Accuracy

The linear beam element was selected for its simplicity and computational speed as opposed to more complex elements such as three dimensional brick elements. By modeling the aircraft wing as a structural beam so beam theory may be used, several geometric limitations are placed on the wing. A major research issue will be to determine the limitations on the wing and to clarify the accuracy of the structural analysis method. By using beam elements, the cross section will be idealized as having the area and moments of inertia of a rectangular solid or box and will not be capable of modeling a curved airfoil shape.

The linear Finite Element Analysis is fairly accurate for a beam which is in

bending and has small deflections. If large torsional loads are applied, a highly twisted wing is used, or the deflections are large, it may be necessary to use nonlinear analysis to obtain an accurate solution. Linear beam theory also ignores the stiffening effect produced with large deformations. If the material used for the wing is highly flexible, a linear analysis will not be sufficient. A flexible material will also exhibit coupling between the two transverse bending degrees of freedom which must be accounted for in the off-diagonal terms within the stiffness matrix.

The Finite Element Model will include various wing geometric parameters which could invalidate the linear beam theory assumption if the parameters become too large. If the thickness and chord length become very large when compared to the wingspan or if the twist angle becomes large, linear beam theory will no longer hold. A highly swept wing under aerodynamic loading will exhibit bending and torsion coupling, but basic beam theory FEA will assume these parameters are uncoupled. The cantilevered boundary conditions of a highly swept wing may also not be accounted for using beam theory because there may be significant differences between the stress concentrations of the forward and aft sections near the root chord of an actual wing. The bending and torsion coupling and the boundary conditions lead to limitations on the maximum sweep angle [26]. If morphing is achieved by deforming the structure so the sweep and dihedral angles undergo large changes compared to their undeformed angles, linear beam theory will also no longer hold. The research will need to determine the limitations of the aforementioned parameters. The research will need to quantify the limitations as well as the accuracy associated with changing each parameter. It will likely be necessary to compare the analysis findings with those of a commercial FEA program which uses fully three dimensional elements or nonlinear beam analysis for several different wing configurations. By comparing with a more accurate FEA program, a numerical quantity can be determined for the accuracy of

the finite element code.

## 3. Modeling of Aeroelastic Effects

1. The research must successfully use the structural analysis in conjunction with the aerodynamic analysis and determine a deflected wing shape. The loads which will be input into the FEA code will be generated by a specific doublet panel aerodynamic code which was developed in MATLAB for the morphing problem. When the FEA determines a deflected wing shape, the new shape will have a different set of aerodynamic loads. An iterative method of alternating between the aerodynamic and structural codes will be necessary to converge on a final deflected shape for the wing. The process for this iterative approach will need to be determined and it will be a critical aspect of the research.

2. The aerodynamic code was not developed to accept a curved, deflected wing shape. The aerodynamic code is set up so that the wing parameters such as the dihedral and sweep angles are single inputs, and it assumes the wing is straight. This means that the output shape determined by the FEA code will not be accurately represented in the aerodynamic code during the iterations. It will likely be necessary to determine effective changes in the sweep and dihedral angles which can approximate the deflection. Although the aerodynamic and aeroelastic properties of a deflected wing are different than those of a straight wing, the deflections will be small and it may be accurate to represent the deflected wing with a straight wing. This method will allow for the use of iterations to converge upon a deflected wing shape.

## D. Research Objectives, Scope, and Methodology

This section describes the objectives and scope of the research and outlines the plan and methodology to achieve these goals.

### 1. Research Objectives and Scope

The objective is to develop a method and computational tool to analyze the structural and aeroelastic effects exhibited by a wing with geometry changes up to 30%. The structural tool must determine the deflections and stresses for a given wing configuration and must work with an existing constant strength source doublet panel method aerodynamic code which provides aerodynamic loads [1], [2]. The aerodynamic and structural tools must be integrated to converge on a deflected wing shape, providing insight into the quasi-static aeroelastic properties of the wing. The stresses calculated by the FEA tool along with the structural limitations for the wing material must ultimately be used by Machine Learning tools [3], [4], [5], [6], [7]. These tools determine the optimum morphing configurations to give the best aerodynamic characteristics while also maintaining the structural integrity of the wing.

Although commercial FEA tools exist which are capable of yielding the required structural analysis results, an in-house FEA code should be developed so it may be easily integrated with the existing tools and modified to account for future requirement changes. Because the existing Machine Learning and aerodynamic tools were developed using MATLAB, the structural tool should also be developed in MATLAB so all of the tools are compatible.

An important aspect will be to quantify the accuracy of the structural tool because it uses various assumptions which are inherent in beam theory, as mentioned in the Research Issues section. The accuracy must be used to determine the ranges

of the morphing parameters where the FEA tool can accurately represent the wing. The structural tool must provide results accurate within 10% when compared to an actual aircraft in order for the tool to be reasonably utilized for future morphing wing modeling purposes.

The scope of the research investigates several significant aspects of the morphing wing problem. The structural and aerodynamic tools must be capable of analyzing the following:

1. Variable wing geometry
    (a) Sweep angle
    (b) Dihedral angle
    (c) Incidence angle and twist
    (d) Taper ratio
    (e) Thickness
    (f) Aspect ratio
2. Aerodynamic Tool
    (a) Low speed, inviscid, and incompressible flow
    (b) NACA 4-Series root and tip airfoils
    (c) Output aerodynamic loads
3. Structural Tool
    (a) Box or solid wing cross section
    (b) Output deflections and rotations
    (c) Output axial stress

Once the Space Frame Finite Element tool is developed, the questions to be investigated are:

1. Can the structural and aerodynamic codes be used in conjunction through an iterative approach to show the quasi-static aeroelastic properties of a deflected morphing wing? The limitations of the aerodynamic code, as discussed the Research Issues section, will need to be considered.

2. How can the structural and aerodynamic codes be accurately and efficiently integrated to produce results which will be of practical use for the Machine Learning tools?

3. What are the limitations of the FEA code due to the various assumptions from using linear analysis and beam theory? How can the accuracy with these limitations be quantified? Limitations on the deflections as well as the geometric morphing parameters must be established.

4. Is the FEA tool correctly yielding the expected linear Euler-Bernoulli beam theory results?

## 2. Method

A commercial FEA program, Abaqus, will be used to develop several comparison cases to validate that the FEA code is generating the correct results. Using linear Euler-Bernoulli beam analysis in Abaqus, the structural tool, which also uses linear Euler-Bernoulli beam analysis, will be validated for the following load cases:

1. Pure bending due to lift or drag

2. Pure torsion due to aerodynamic moment

There are many limitations associated with a linear FEA code which uses Euler-Bernoulli beam elements. In order to quantify the accuracy associated with the code, Abaqus will be used to develop several comparison wing models. Timoshenko beam theory is capable of accounting for shear deformations and is a more accurate beam model than Euler-Bernoulli beam theory. The structural tool will be compared to pure bending and pure torsion cases modeled using Timoshenko beam theory to verify the accuracy of the structural tool. One of the assumptions inherent in linear analysis is that the deflections are small when compared to the overall scale of the structure. By using nonlinear beam analysis in Abaqus, a more accurate representation of the wing will be observed. The test cases will consist of various flexural stiffnesses to determine if the given cases are within the linear range. By comparing the results between the Abaqus model and the Space Frame FEA code, an estimate of the structural tool accuracy for each case will be determined. As the deflections increase with higher load magnitudes, the associated accuracy will decrease.

Because a swept wing under aerodynamic loading experiences bending and torsion coupling and the cantilevered boundary conditions become more complex, 3D brick elements should be used in Abaqus to analyze the accuracy of the structural tool for a swept wing case. By using various sweep angle cases, the sweep angle limitations for the tool will be determined. Because beam theory is only valid for long, slender beams, 3D elements may also be used to create various aspect ratio wings to test the limitations on the aspect ratio. A real world aircraft wing has a more complex internal structure than a beam. The structure may have various materials and structural components such as spar caps, spar shear webs, ribs, skin, and a wing carry-through structure. An Abaqus model of a real wing should be compared to the structural tool. The verification cases are shown below:

1. Timoshenko Beam Model using Abaqus
    (a) Pure bending due to lift or drag
    (b) Pure torsion due to aerodynamic moment
2. Nonlinear Beam Analysis using Abaqus
    (a) Pure bending due to only lift or drag
    (b) Pure torsion due to aerodynamic moment
3. 3D Brick Element Analysis with Full Aerodynamic Loading using Abaqus
    (a) Various sweep angles
    (b) Various aspect ratios
4. Complex Wing Model using Abaqus
    (a) Various structural tool stiffnesses
    (b) Various structural tool boundary conditions

The code integration issue will be addressed by developing an overarching computer code which will be used to organize the interaction of the aerodynamic and structural tools. These tools must be setup as function files which may be accessed by the main program. The main program must first establish the values of the morphing parameters for the current wing configuration as discussed in Section I. The morphing parameters will then be used as inputs to the aerodynamic and structural tools.

The aerodynamic tool must be utilized first to output values necessary to calculate the force and moment loads acting on the wing. The doublet panel method uses a grid which covers the upper and lower surfaces of the wing, and the grid is divided

into chordwise and spanwise panels for both the left and right sides of the wing. Because the aerodynamic tool is setup to calculate the lift and moment coefficients at each panel and the total drag coefficient, the main program will need to modify the aerodynamic coefficients to obtain the lift, drag, and pitching moment loads acting on each element. Beam elements are used in the structural tool, so there is only one element for each span station. The chordwise lift and moment values must be combined for each span station, so only one lift force and pitching moment is applied to each element. The total drag force will be proportionally applied to each element.

The structural tool will use the geometric morphing parameters along with the lift, drag, pitching moment, and load locations as inputs. The tool will be setup so the element spacing is tied to the panel spacing of the aerodynamic tool. Because the structural tool will solve a cantilevered beam problem, it can only handle half of the wing at a time. The main program must call the structural tool function twice to obtain the deflection and axial stress values for the entire wing. These values along with the aerodynamic coefficients may be used by various Machine Learning tools to determine the next morphed wing shape needed for aerodynamic effectiveness and wing structural integrity. The aerodynamic and structural tool integration process is described below:

1. An overarching main program will integrate the aerodynamic and structural tools

2. Input morphing geometry parameters must be selected

3. The aerodynamic tool function file will be called using the morphing geometry inputs and it will output aerodynamic coefficients

4. The main program will modify the aerodynamic coefficients to obtain lift, drag,

and pitching moment loads at each spanstation

5. The structural tool function file will be called once for each half span of the wing using the morphing wing geometry, loads, and load locations as inputs and it will output the wing deflections and axial stresses

6. The aerodynamic coefficients, wing deflections, and stresses may be used by Machine Learning tools to determine the next morphed wing geometry

An iterative approach which incorporates the structural and aerodynamic tools may show more realistic quasi-static aeroelastic deflections. Each iteration will calculate the aerodynamic loads and the structural deflections due to those loads. The iterations will use the new deflected geometry found during the previous iteration to generate new aerodynamic loads. The rotation deflections cause a change in the twist angle of the wing, so an updated twist angle will be used as an input to the aerodynamic tool. Because the aerodynamic code was not designed to handle a curved, deflected wing, the bending deflections will need to be converted to an approximate change in the dihedral and sweep angles. The maximum deflection is located at the wing tip, so the maximum adjusted dihedral and sweep angles may be determined using the angle between the wing root and wing tip. These adjusted dihedral and sweep angles will be used as inputs for the aerodynamic code. Modified wing span and aspect ratio values should be calculated to account for the new dihedral and sweep angles, and these values should also be used as inputs for the aerodynamic tool. This iteration process can be continued until a converged, deflected wing shape is observed. The steps for the iterative quasi-static linear aeroelastic analysis method are shown as follows:

1. Choose initial wing geometry
2. Run aerodynamic tool to obtain aerodynamic loads based on initial geometry
3. Run structural tool using aerodynamic loads to determine deflected geometry
4. Determine the modified twist angle and the approximate dihedral angle, sweep angle, wing span, and aspect ratio
5. Run aerodynamic tool using the new wing geometry
6. Run structural tool using the new aerodynamic loads to determine a new deflected geometry
7. Repeat Steps 4-6 until the process converges on a deflected wing geometry

Figure 8 below shows the steps for the aeroelastic analysis method in a flow chart.

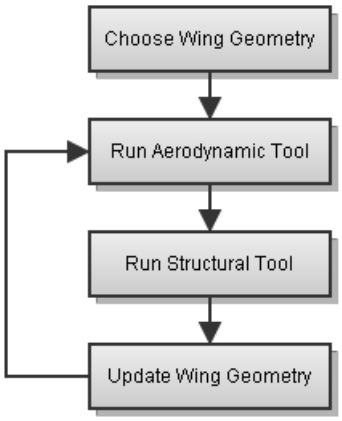


Fig. 8. Iterative Aerodynamic and Structural Interaction

# 3. Contributions of This Research

This research is novel and represents a fundamental advance for several reasons. It applies Finite Element Analysis to the morphing wing problem and uses an iterative method to incorporate the aerodynamic and structural effects which is a unique approach for morphing applications. Also, this research develops the strucutral tool in a way that allows it to easily interface with other existing morphing and Machine Learning tools. The use of the structural tool in morphing research is a new and unique approach to learning about the structural impacts and limitations of a reconfigurable wing.

# CHAPTER II

# FINITE ELEMENT ANALYSIS

This chapter will discuss the selection of the structural analysis method, derive the necessary equations and theory, and discuss the limitations of the chosen approach.

## A. Selection of Structural Analysis Method

Because a fully morphing aircraft can have an infinite number of wing configurations, it would be too expensive and unrealistic to use the typical commercial finite element tools which utilize 3-D modeling software. A new model would need to be created for every different wing configuration. For this reason, a Finite Element Analysis (FEA) code was selected as the most versatile tool for structural analysis of a morphing air vehicle.

The major types of elements in FEA include beam, shell, and three-dimensional brick elements. The beam model is the simplest because it reduces the structural element to one independent spacial variable [28]. In order to simplify the problem, a beam model of FEA was selected for the structural analysis method used in this research. Linear and nonlinear analysis methods can be used for beam FEA. The former is accurate if the material is in the linear elastic range and the changes in geometry are small, and it is computationally simpler than nonlinear analysis. For this reason, a linear analysis approach was selected for the FEA method used in the research.

This chapter will discuss a specific type of linear beam FEA model known as Space Frame Finite Element Analysis. A space frame is a structure with members which may have any orientation in three dimensional space and may have forces and moments in all directions at each elemental node, so there are six degrees of

freedom per node. A two-noded element is the simplest and most common type of beam element, and with a two-noded element there will be nodal displacements and rotations in all directions at either end of every element. It is possible to use linear FEA to approximate the structural effects of a wing by modeling the wing as a cantilevered beam that has small deflections assuming that the wing is an Euler-Bernoulli beam, isotropic, and homogeneous. This means the cross-sections remain planar and normal to the neutral axis, the properties are the same in all directions, and there is a consistent material throughout. One of the limitations of Euler-Bernoulli beam theory is that it is only accurate when modeling beams with a length to thickness ratio of 15 to 1 or greater, where the thickness is in the direction of loading [30]. Unique dimensions, properties, and orientations for every element may be specified to allow for the geometry of a morphed wing configuration.

## B. Development of Finite Element Analysis Equations

This section discusses the theory of general FEA for space frames and shows the derivation of the necessary equations. The approach follows methods and nomenclature similar to that of Weaver in [25] and [27] as well as Haisler in [24].

### 1. Virtual Work Development of Finite Element Analysis

This subsection follows the methods shown in [25] . The generic displacements may be defined within the element as the column vector $\mathbf{u}$

$$\mathbf{u} = \{u,\ v,\ w,\ \theta_x,\ \theta_y,\ \theta_z\} \tag{2.1}$$

where $u$, $v$, and $w$ are the $x$, $y$, and $z$ displacements, respectively. $\theta$ is the small rotation about the axis shown in the subscript. $\theta_y$ and $\theta_z$ are the derivatives with

respect to $x$ of $w$ and $v$, respectively. The vector $\mathbf{q}_e$ gives the displacements and rotations at each node within the element. For a two-noded element, $\mathbf{q}_e$ is given by the following column vector

$$\mathbf{q}_e = \{u_1,\ v_1,\ w_1,\ \theta_{x1},\ \theta_{y1},\ \theta_{z1},\ u_2,\ v_2,\ w_2,\ \theta_{x2},\ \theta_{y2},\ \theta_{z2}\} \tag{2.2}$$

where the 1 and 2 subscripts denote the left and right nodes, respectively. The interpolation function or shape function, $\mathbf{N}$, relates $\mathbf{u}$ and $\mathbf{q}_e$ by the following equation.

$$\mathbf{u} = \mathbf{N}\mathbf{q}_e \tag{2.3}$$

The strain vector, $\boldsymbol{\epsilon}$, may be related to the displacements using a matrix $\mathbf{d}$ which is a linear differential operator as shown below.

$$\boldsymbol{\epsilon} = \mathbf{d}\mathbf{u} \tag{2.4}$$

Substituting Equation 2.3 into 2.4 yields

$$\boldsymbol{\epsilon} = \mathbf{d}\mathbf{N}\mathbf{q}_e = \mathbf{B}\mathbf{q}_e \tag{2.5}$$

where $\mathbf{B}$ is the matrix that gives the strains at any point in the element due to the nodal displacements. The stress-strain relationship is defined using the following equation

$$\boldsymbol{\sigma} = \mathbf{E}\boldsymbol{\epsilon} \tag{2.6}$$

where $\mathbf{E}$ is the constitutive matrix relating the strains to the stress vector, $\boldsymbol{\sigma}$. For derivation purposes, the properties shown in this subsection, such as $\boldsymbol{\epsilon}$ and $\mathbf{E}$, include the full characteristics of a general structure and are vectors and matrices, respectively. In the following subsection, these properties will be simplified using assumptions which include small strain theory and Euler-Bernoulli beam theory.

The principle of virtual work states that the virtual work of external actions is equal to the virtual strain energy of internal stresses for a structure in equilibrium which is subjected to small virtual displacements. The following equation shows the principle of virtual work for a finite element

$$\delta U_e = \delta W_e \tag{2.7}$$

where $\delta U_e$ is the virtual strain energy due to internal stresses within an element and $\delta W_e$ is the virtual work due to external forces on the element. Equation 2.3 may be written in terms of virtual displacements as

$$\delta \mathbf{u} = \mathbf{N} \delta \mathbf{q}_e \tag{2.8}$$

Similarly, Equation 2.5 may be written in terms of virtual strains and displacements as

$$\delta \boldsymbol{\epsilon} = \mathbf{B} \delta \mathbf{q}_e \tag{2.9}$$

The virtual strain energy may be written in terms of stress and strain as

$$\delta U_e = \int_V \delta \boldsymbol{\epsilon}^T \boldsymbol{\sigma} dV \tag{2.10}$$

and the virtual work may be written in terms of the nodal boundary loads vector $\mathbf{P}_e$ and distributed body loads vector $\mathbf{f}$.

$$\delta W_e = \delta \mathbf{q}_e{}^T \mathbf{P}_e + \int_V \delta \mathbf{u}^T \mathbf{f} dV \tag{2.11}$$

By substituting Equations 2.10 and 2.11 into Equation 2.7, the following equation is obtained:

$$\int_V \delta \boldsymbol{\epsilon}^T \boldsymbol{\sigma} dV = \delta \mathbf{q}_e{}^T \mathbf{P}_e + \int_V \delta \mathbf{u}^T \mathbf{f} dV \tag{2.12}$$

By manipulating Equation 2.12 with Equations 2.5, 2.6, 2.8, and 2.9, the following

equation is found:

$$\left(\int_V \mathbf{B}^T\mathbf{E}\mathbf{B}dV\right)\mathbf{q}_e = \mathbf{P}_e + \int_V \mathbf{N}^T\mathbf{f}dV \tag{2.13}$$

which may be rewritten as

$$\mathbf{K}_e\mathbf{q}_e = \mathbf{P}_e + \mathbf{Q}_e \tag{2.14}$$

where $\mathbf{K}_e$ is the elemental stiffness matrix as shown below

$$\mathbf{K}_e = \int_V \mathbf{B}^T\mathbf{E}\mathbf{B}dV \tag{2.15}$$

and $\mathbf{Q}_e$ is the vector of equivalent nodal loads due to the distributed loads vector as seen below.

$$\mathbf{Q}_e = \int_V \mathbf{N}^T\mathbf{f}dV \tag{2.16}$$

2. Space Frame Stiffness Matrix and Equivalent Nodal Load Formulation

The approach in this section follows methods and nomenclature similar to that of Weaver in [25]. Space Frame FEA uses beam elements which exhibit displacements and rotations in any direction. Also, each element may have a unique local axis orientation when compared to the neighboring elements. The elemental stiffness matrices are determined by combining the stiffnesses which correspond to the axial, flexural, and torsional elements.

An axial element is an element which may only experience $u$ displacements due to loads in the local $x$ direction. The displacements may be assumed to vary linearly with $x$ within the element, and the following linear equation can be used to ensure monotonic convergence of the solution:

$$u = c_1 + c_2x \tag{2.17}$$

Using the element boundary conditions $u(0) = q_1$ and $u(L) = q_7$, where $L$ is the

element length and the $q_1$ and $q_7$ correspond to indices 1 and 7 within Equation 2.2, Equation 2.17 may be solved in terms of the interpolation function $\mathbf{N}$ as shown in Equation 2.18

$$u = q_1 + \frac{q_7 - q_1}{L}x = \left[1 - \frac{x}{L},\ \frac{x}{L}\right]\begin{bmatrix} q_1 \\ \\ q_7 \end{bmatrix} = \mathbf{N}\mathbf{q}_{e,\ axial} \tag{2.18}$$

where

$$\mathbf{N} = \left[1 - \frac{x}{L},\ \frac{x}{L}\right] \tag{2.19}$$

$\mathbf{B}$ may be written as the derivative of $\mathbf{N}$ with respect to $x$ for the axial element, and $\mathbf{E}$ is the constant $E$, the elastic modulus which relates the axial stress and axial strain. Using Equation 2.19 and the mentioned simplifications for $\mathbf{B}$ and $\mathbf{E}$, Equation 2.15 may be written as the axial entries of the elemental stiffness matrix and shown by the following equation

$$\mathbf{K}_{e,\ axial} = \int_0^L EA_x \frac{d\mathbf{N}_j}{dx}\frac{d\mathbf{N}_i}{dx}dx \quad \text{for } i = 1, 7 \text{ and } j = 1, 7 \tag{2.20}$$

where $A_x$ is the cross-sectional area which is perpendicular to the neutral axis of the beam.

The flexural components of the elemental stiffness matrix may be developed in a similar manner. A beam in bending experiences transverse displacements and small rotations at each node. The assumed displacement function must be cubic to account for the displacement and rotation boundary conditions at both $x = 0$ and $x = L$. Considering bending about the $z$ axis, the beam will have displacements, $v$, and rotations, $\theta_z$, which correspond to the indices 2, 6, 8, and 12 of the nodal displacements and rotations given in Equation 2.2. The displacement function for bending about the $z$ axis which ensures monotonic convergence of the solution is

shown below.

$$v = c_1 + c_2 x + c_3 x^2 + c_4 x^3 \tag{2.21}$$

Using the boundary conditions to solve for the constants in Equation 2.21 as done previously in 2.18, the following interpolation function for bending about the $z$ axis is found:

$$\mathbf{N} = \left[1 - 3\frac{x^2}{L^2} + 2\frac{x^3}{L^3},\ x - 2\frac{x^2}{L} + \frac{x^3}{L^2},\ 3\frac{x^2}{L^2} - 2\frac{x^3}{L^3},\ -\frac{x^2}{L} + \frac{x^3}{L^2}\right] \tag{2.22}$$

Because the flexural strain is a function of the curvature, or second derivative of $v$ with respect to $x$, Equation 2.15 may be written for the flexural components of the stiffness matrix as follows:

$$\mathbf{K}_{e,\ flexural} = \int_0^L EI_z \frac{d^2\mathbf{N}_j}{dx^2}\frac{d^2\mathbf{N}_i}{dx^2}dx \quad \text{for } i = 2, 6, 8, 12 \text{ and } j = 2, 6, 8, 12 \tag{2.23}$$

where

$$I_z = \int_A y^2 dA \tag{2.24}$$

represents the moment of inertia about the $z$ axis. For the case where the cross section is a solid rectangle, $I_z$ is defined as

$$I_z = \frac{bh^3}{12} \tag{2.25}$$

where $b$ is the width along the $z$ direction and $h$ is the height along the $y$ direction. $b$ is not the same as $b$ which is used elsewhere in the thesis to refer to wing span. Equation 2.26 gives $I_z$ for a box cross section

$$I_z \approx \frac{bh^3}{12} - \frac{(b - 2t_w)(h - 2t_f)^3}{12} \tag{2.26}$$

where $t_w$ is the thickness of each of the two box sides which are perpendicular to the $z$ direction and $t_f$ is the thickness of the two sides perpendicular to the $y$ direction.

The same method may be used to determine the flexural elemental stiffness matrix for bending about the $y$ axis, but $w$, $\theta_y$, and $I_y$ are used instead of $v$, $\theta_z$, and $I_z$, respectively. $I_y$ is found for rectangular and box cross sections using Equations 2.27 and 2.28, respectively.

$$I_y = \frac{hb^3}{12} \tag{2.27}$$

$$I_y \approx \frac{hb^3}{12} - \frac{(h-2t_f)(b-2t_w)^3}{12} \tag{2.28}$$

The indices of the stiffness matrix correspond to $i = 3, 5, 9, 11$ and $j = 3, 5, 9, 11$.

For a torsional element, there are only rotations $\theta_x$ about the $x$ axis, so the linear interpolation function in Equation 2.19 may be used. For pure torsion, $\mathbf{E}$ is the constant $G$, the shear modulus of the material. For an isotropic material, $G$ is defined as

$$G = \frac{E}{2(1+\nu)} \tag{2.29}$$

where $\nu$ is the Poisson's ratio of the material. Equation 2.15 may be written as

$$\mathbf{K}_{e,\,torsional} = \int_0^L GJ \frac{d\mathbf{N}_j}{dx}\frac{d\mathbf{N}_i}{dx}dx \quad \text{for } i = 4, 10 \text{ and } j = 4, 10 \tag{2.30}$$

where $J$ is the polar moment of inertia which is approximated as

$$J \approx hb^3\left[\frac{1}{3} - 0.21\frac{b}{h}\left(1 - \frac{b^4}{12h^4}\right)\right] \tag{2.31}$$

for a solid rectangular cross section where $h$ is greater than $b$. $h$ and $b$ must be interchanged in Equation 2.31 if $h$ is less than $b$. For a box cross section, Equation 2.32 is used to calculate $J$.

$$J \approx \frac{[(h-t_f)(b-t_w)]^2(t_f+t_w)}{(b-t_w)+(h-t_f)} \tag{2.32}$$

The elemental stiffness matrix for elements experiencing axial, flexural, and torsional deformations may be formed by combining the three stiffness matrices shown

in Equations 2.20, 2.23, and 2.30. The stiffness matrix is a twelve by twelve matrix because there are six degrees of freedom for each of the two nodes. The matrix, $\mathbf{K}_e$, as shown by Weaver in [27], is presented in Equation 2.33.

The equivalent nodal loads for beam elements which experience axial, flexural, and torsional deformations are found using Equation 2.16 with the interpolation functions shown in Equations 2.19 and 2.22. Equation 2.34 gives the twelve by one column vector for the elemental nodal loads. In Equation 2.34, $f$ is the magnitude of the distributed force per length in the axis direction notated in the subscript and $m_x$ is the distributed moment per length about the local $x$ axis.

$$\mathbf{K}_e = \begin{bmatrix} \frac{EA_x}{L} & 0 & 0 & 0 & 0 & 0 & -\frac{EA_x}{L} & 0 & 0 & 0 & 0 & 0 \\ 0 & 12\frac{EI_z}{L^3} & 0 & 0 & 0 & 6\frac{EI_z}{L^2} & 0 & -12\frac{EI_z}{L^3} & 0 & 0 & 0 & 6\frac{EI_z}{L^2} \\ 0 & 0 & 12\frac{EI_y}{L^3} & 0 & -6\frac{EI_y}{L^2} & 0 & 0 & 0 & -12\frac{EI_y}{L^3} & 0 & -6\frac{EI_y}{L^2} & 0 \\ 0 & 0 & 0 & \frac{GJ}{L} & 0 & 0 & 0 & 0 & 0 & -\frac{GJ}{L} & 0 & 0 \\ 0 & 0 & -6\frac{EI_y}{L^2} & 0 & 4\frac{EI_y}{L} & 0 & 0 & 0 & 6\frac{EI_y}{L^2} & 0 & 2\frac{EI_y}{L} & 0 \\ 0 & 6\frac{EI_z}{L^2} & 0 & 0 & 0 & 4\frac{EI_z}{L} & 0 & -6\frac{EI_z}{L^2} & 0 & 0 & 0 & 2\frac{EI_z}{L} \\ -\frac{EA_x}{L} & 0 & 0 & 0 & 0 & 0 & \frac{EA_x}{L} & 0 & 0 & 0 & 0 & 0 \\ 0 & -12\frac{EI_z}{L^3} & 0 & 0 & 0 & -6\frac{EI_z}{L^2} & 0 & 12\frac{EI_z}{L^3} & 0 & 0 & 0 & -6\frac{EI_z}{L^2} \\ 0 & 0 & -12\frac{EI_y}{L^3} & 0 & 6\frac{EI_y}{L^2} & 0 & 0 & 0 & 12\frac{EI_y}{L^3} & 0 & 6\frac{EI_y}{L^2} & 0 \\ 0 & 0 & 0 & -\frac{GJ}{L} & 0 & 0 & 0 & 0 & 0 & \frac{GJ}{L} & 0 & 0 \\ 0 & 0 & -6\frac{EI_y}{L^2} & 0 & 2\frac{EI_y}{L} & 0 & 0 & 0 & 6\frac{EI_y}{L^2} & 0 & 4\frac{EI_y}{L} & 0 \\ 0 & 6\frac{EI_z}{L^2} & 0 & 0 & 0 & 2\frac{EI_z}{L} & 0 & -6\frac{EI_z}{L^2} & 0 & 0 & 0 & 4\frac{EI_z}{L} \end{bmatrix} \tag{2.33}$$

$$\mathbf{Q}_e = \begin{bmatrix} \frac{1}{2}f_x L \\ \frac{1}{2}f_y L \\ \frac{1}{2}f_z L \\ \frac{1}{2}m_x L \\ -\frac{1}{12}f_z L^2 \\ \frac{1}{12}f_y L^2 \\ \frac{1}{2}f_x L \\ \frac{1}{2}f_y L \\ \frac{1}{2}f_z L \\ \frac{1}{2}m_x L \\ \frac{1}{12}f_z L^2 \\ -\frac{1}{12}f_y L^2 \end{bmatrix} \tag{2.34}$$

### 3. Space Frame Axis Orientation and Transformation

The approach in this section follows methods and nomenclature similar to that of Weaver in [27]. In the previous section, the equations for the elemental stiffness matrix, $\mathbf{K}_e$, and equivalent nodal loads, $\mathbf{Q}_e$, were developed with respect to the local coordinate axes. In order to assemble all of the elements and analyze the entire structure, each element must first be transformed into the global coordinate system. The figure below, taken from [27], shows the orientation of the element with respect to the global coordinates $x_s$, $y_s$, and $z_s$. As shown in Figure 9, the local coordinate axis must be rotated by angles $\alpha$, $\beta$, and $\gamma$ to transform the element into the global coordinates. The following direction cosine matrices are utilized to transform the

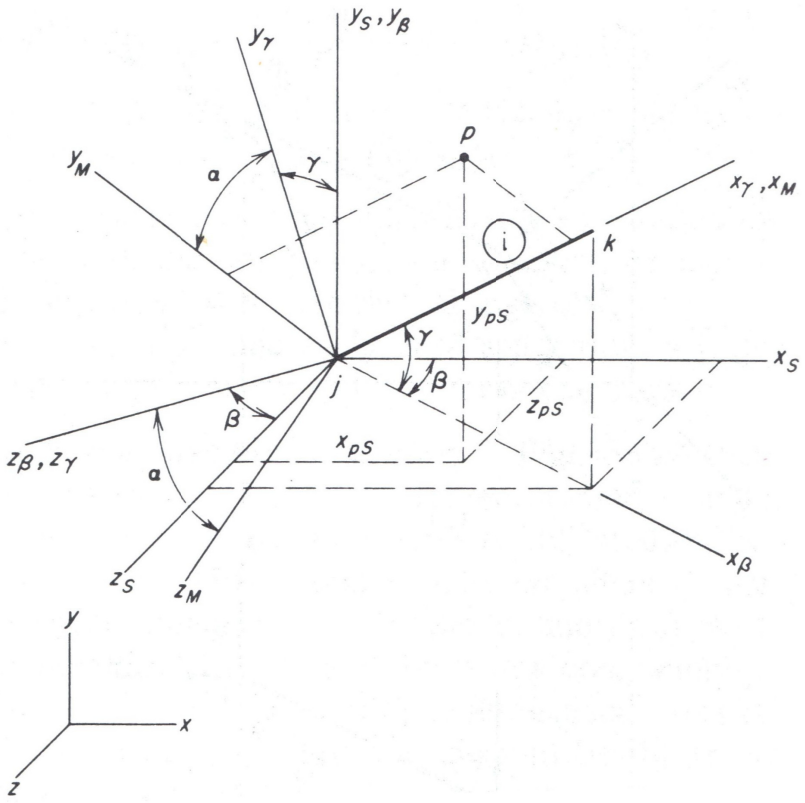


Fig. 9. Rotation of Axes for a Space Frame Member [27]

coordinates about each rotation angle:

$$\mathbf{R}_\alpha = \begin{bmatrix} 1 & 0 & 0 \\ 0 & \cos\alpha & \sin\alpha \\ 0 & -\sin\alpha & \cos\alpha \end{bmatrix} \tag{2.35}$$

$$\mathbf{R}_\beta = \begin{bmatrix} \cos\beta & 0 & \sin\beta \\ 0 & 1 & 0 \\ -\sin\beta & 0 & \cos\beta \end{bmatrix} \tag{2.36}$$

$$\mathbf{R}_\gamma = \begin{bmatrix} \cos\gamma & \sin\gamma & 0 \\ -\sin\gamma & \cos\gamma & 0 \\ 0 & 0 & 1 \end{bmatrix} \tag{2.37}$$

The negative sign occurs in Equation 2.36 in the lower left corner as opposed to the upper right corner because $\beta$ is a negative rotation about the $y_S$ axis shown in Figure 9. The rotation matrix may be formed by combining the direction cosine matrices using the equation shown below.

$$\mathbf{R} = \mathbf{R}_\alpha \mathbf{R}_\beta \mathbf{R}_\gamma \tag{2.38}$$

The elemental stiffness matrices and the equivalent nodal load vectors must be transformed into the global coordinates. $\mathbf{K}_e$ is a twelve by twelve matrix and $\mathbf{Q}_e$ is a twelve by one vector, but Equation 2.38 yields a three by three matrix. The following equation gives the necessary twelve by twelve rotation matrix:

$$\mathbf{R}_T = \begin{bmatrix} \mathbf{R} & 0 & 0 & 0 \\ 0 & \mathbf{R} & 0 & 0 \\ 0 & 0 & \mathbf{R} & 0 \\ 0 & 0 & 0 & \mathbf{R} \end{bmatrix} \tag{2.39}$$

The elemental stiffness matrix is transformed from the local coordinates to the global coordinates using the equation

$$\mathbf{K}_{e,\,global} = \mathbf{R}_T^T \mathbf{K}_{e,\,local} \mathbf{R}_T \tag{2.40}$$

and the elemental equivalent nodal loads vector is transformed using the equation below.

$$\mathbf{Q}_{e,\,global} = \mathbf{R}_T^T \mathbf{Q}_{e,\,local} \tag{2.41}$$

### 4. Assembly of the Global Stiffness Matrix and Solution

Once the elemental stiffness matrices and equivalent nodal loads are transformed into the global coordinate system, the stiffness matrix and equivalent nodal loads for the structure are assembled, the displacement and rotation boundary conditions are applied, and the overall structure is analyzed. To develop the necessary equations, the principle of virtual work for the structure, as described in [25], is shown below

$$\delta U_s = \delta W_s \tag{2.42}$$

where the subscript $s$ denotes that the term applies to the entire structure. Following a similar approach as Subsection 1, the following equation relating the stiffness, displacements, and loads for the overall structure is found:

$$\mathbf{Kq} = \mathbf{P} + \mathbf{Q} \tag{2.43}$$

where $\mathbf{K}$ is the assembled stiffness matrix for the structure, $\mathbf{q}$ is the nodal displacement column vector for the structure, $\mathbf{P}$ is the column vector of external point loads applied to nodes of the structure, and $\mathbf{Q}$ is the assembled equivalent nodal loads for the structure.

The notation and methods shown below are similar to those used by Haisler in [24]. To determine $\mathbf{K}$, the $\mathbf{K}_e$ for every element must be combined. Because there are six degrees of freedom per node and two nodes per element, the elemental stiffness matrix may be subdivided into four quadrants with each quadrant consisting of a six by six matrix. An example of the subdivided elemental stiffness matrix is shown below

$$\mathbf{K}_e{}^1 = \begin{bmatrix} \mathbf{K}_{11}{}^1 & \mathbf{K}_{12}{}^1 \\ \mathbf{K}_{21}{}^1 & \mathbf{K}_{22}{}^1 \end{bmatrix} \tag{2.44}$$

where the subscripts denote the quadrant location and the superscript denotes the

element number. For two elements sharing the same node, the corresponding nodal entries of the element stiffness matrices must be summed. An example of assembling the stiffness matrix for adjacent elements 1 and 2 which are arranged with the right end element 1 connected to the left end of element 2 is shown below.

$$\mathbf{K} = \begin{bmatrix} \mathbf{K}_{11}{}^{1} & \mathbf{K}_{12}{}^{1} & 0 \\ \mathbf{K}_{21}{}^{1} & \mathbf{K}_{22}{}^{1} + \mathbf{K}_{11}{}^{2} & \mathbf{K}_{12}{}^{2} \\ 0 & \mathbf{K}_{21}{}^{2} & \mathbf{K}_{22}{}^{2} \end{bmatrix} \tag{2.45}$$

If there are $n$ elements and every element is arranged end to end starting with element 1 and ending with element $n$, the above example may be continued to assemble the stiffness matrix for the structure. The overall matrix size is $6(n+1)$ by $6(n+1)$.

Similarly, the elemental equivalent nodal loads may be subdivided into the loads for each node as shown below

$$\mathbf{Q}_{e}{}^{1} = \begin{bmatrix} \mathbf{Q}_{1}{}^{1} \\ \mathbf{Q}_{2}{}^{1} \end{bmatrix} \tag{2.46}$$

where $\mathbf{Q}_{1}{}^{1}$ and $\mathbf{Q}_{2}{}^{1}$ are six by one column vectors for the element 1 equivalent nodal loads on the left and right nodes, respectively. For the case described in the example given in Equation 2.45, the example below shows how the equivalent nodal loads may be assembled.

$$\mathbf{Q} = \begin{bmatrix} \mathbf{Q}_{1}{}^{1} \\ \mathbf{Q}_{2}{}^{1} + \mathbf{Q}_{1}{}^{2} \\ \mathbf{Q}_{2}{}^{2} \end{bmatrix} \tag{2.47}$$

The process shown in Equation 2.47 may be continued for $n$ elements if the elements are arranged end to end as described above. The length of vector $\mathbf{Q}$ will be $6(n+1)$ by one.

The displacement and rotation boundary conditions applied to the structure, such as a cantilevered or pinned location, must be satisfied before the structure can

be analyzed. One method of accounting for these restrictions is to add an extremely large number to the assembled stiffness matrix indices which corresponds to the nodal degree of freedom which is restricted. This method gives a nearly infinite stiffness in the necessary degrees of freedom at the particular node. After $\mathbf{K}$ is modified to account for the displacement and rotation boundary conditions, Equation 2.43 may be solved for the vector $\mathbf{q}$. The nodal displacements throughout the structure are now known.

## 5. Post Processing and Axial Stress Analysis

Once the nodal displacements, $\mathbf{q}$, are found for the structure, the individual elemental nodal displacements, $\mathbf{q}_e$, are easily located within $\mathbf{q}$ in groupings of twelve. By using the interpolation functions from Equations 2.19 and 2.22 with Equation 2.3, the displacements and rotations throughout each element are found.

The elemental boundary loads are found by solving Equation 2.14 for $\mathbf{P}_e$ using the newly found $\mathbf{q}_e$. In order to analyze the stresses within each element, the elemental boundary forces must first be converted from the global coordinate system into the local coordinates. The following equation may be used to transform the loads into local system:

$$\mathbf{P}_{e,\,local} = \mathbf{R}_T \mathbf{P}_{e,\,global} \tag{2.48}$$

With the elemental boundary loads in the local coordinates, the following equation from Haisler in [24] may be used to determine the axial stress, $\sigma_{xx}$, throughout the element:

$$\sigma_{xx} = \frac{P}{A_x} - \frac{M_z y}{I_{zz}} + \frac{M_y z}{I_{yy}} \tag{2.49}$$

where $y$ and $z$ span across the height and width of the cross section, respectively, in the local coordinate system with the origin located at the principal axis. $P$, $M_y$,

and $M_z$ are terms within the vector $\mathbf{P}_e$. Equations 2.48 and 2.49 may be used for all elements to determine the internal loads and axial stresses throughout the entire structure.

## C. Assumptions

This chapter describes a linear beam FEA approach which contains many inherent assumptions regarding the structural element. Because beam analysis is used, the $x$ dimension of each element must be significantly larger than the other two dimensions. This means that the element must be long and slender. If the structure is composed of elements which are arranged end to end as described above, then the elemental geometric limitations become limitations of the overall structure. Because a linear analysis method was selected, the displacements and rotations must be small when compared to the overall size of the structure and the material cannot be highly flexible.

As described by Pai in [28], there are three types of beam theories: the Euler-Bernoulli beam theory, the shear-deformable beam theories, and the three-dimensional stress beam theories. The method used in this research is Euler-Bernoulli beam theory, so only the axial stress, $\sigma_{xx}$, is considered and the cross sections are assumed to remain plane and perpendicular to the reference axis after deformation. For the flexural components, the transverse shear stresses and both in-plane and out-of-plane warpings are neglected. For the torsional components, only the shear stresses are considered. The Euler-Bernoulli approach accounts for only one of the six stress states. The chosen method is accurate if the deflections and rotations are small and the coupling effects between bending and twisting motion are insignificant.

By assuming the structure is composed of a homogeneous and isotropic material, each element must have a uniform material throughout and the material properties

must be the same in all directions. This means that it is not possible to accurately analyze a composite, anisotropic structure using the methods described in this chapter. It should be noted that a beam model uses the cross-sectional area and moments of inertia, but it does not model the actual shape of the cross section.

# CHAPTER III

## SPACE FRAME FINITE ELEMENT ANALYSIS COMPUTATIONAL TOOL DEVELOPMENT

This chapter describes the implementation of the Space Frame Finite Element Analysis decribed in the previous chapter. The structural analysis computational tool main program and subroutines are discussed. Flow charts are used throughout this chapter to show the basic program operations. For a more detailed understanding of the code operations, the full MATLAB code for the structural tool is included as a supplemental file attached to this thesis.

### A. Structural Tool Main Program

The organization of the structural tool main program, STRUCTURES, is shown in flow chart form in Figure 10. The first set of inputs specifies the wing geometry and loads. The geometry includes the wing span, aspect ratio, chord length taper ratio, thickness taper ratio, root thickness as a percentage of the root chord length, root incidence angle, tip incidence angle, leading edge sweep angle, and dihedral angle. The chord taper ratio and thickness taper ratio, as shown by $\lambda_{chord}$ and $\lambda_{thickness}$, are the ratios of $c_t$ to $c_r$ and $t_t$ to $t_r$, respectively.

The loads are input as a structure array which includes vectors of the lift, drag, pitching moment, and load application coordinates. The individual element lengths and node placement depend upon the load application coordinates. The program is setup to analyze half of the wing at a time. If the left and right halves of the wing are different, the program may be run twice, once for each half of the wing. The coordinate axis was previously shown in Figure 9. Although aerodynamic loads are distributed across the area of the wing, for this program they must be input as point

loads applied to the principal axis of the wing. A subroutine will later convert these point loads into distributed loads over the length of each element. True point loads may be included separately in the loads structure array. The weight is not included as a load input because it will be calculated later using the material density.

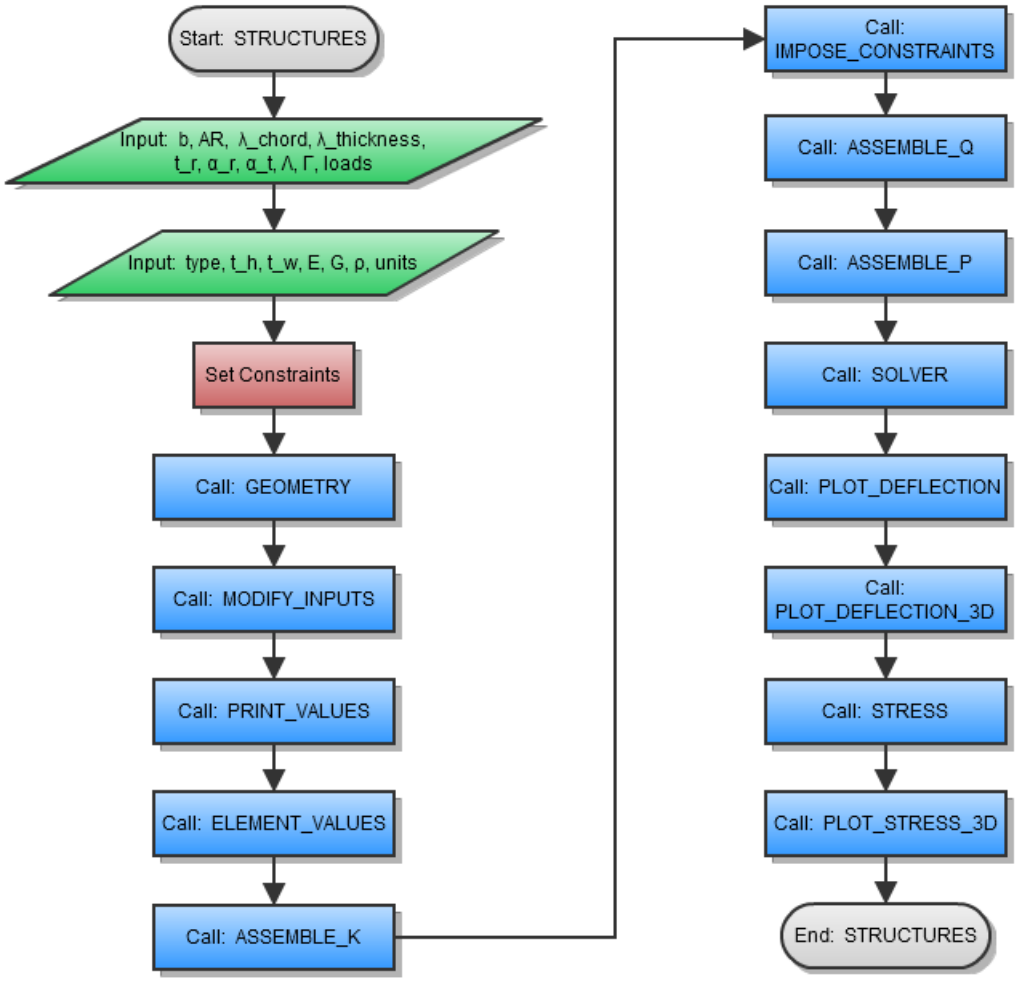


Fig. 10. Structural Tool Main Program

The next set of inputs specifies whether the cross section type is a solid rectangle or a box. If it is a box cross section, the box thicknesses $t_h$ and $t_w$ must be included,

where $t_h$ is the thickness of the top and bottom portions of the box cross section and $t_w$ is the thickness of each side portion of the box cross section. The inputs also include the material elastic modulus, shear modulus, and density. The units must be specified as English or metric. Inches and pounds are used if English units are selected and meters and Newtons are used for metric.

Because the tool is designed specifically for a wing, a cantilever constraint is specified for the root of the wing. The final section of the main program includes all of the subroutine calls.

## B. Structural Tool Subroutines

This section describes all of the subroutines which are called by the structural tool main program. The subroutines prepare the inputs for analysis, implement the equations given in the previous chapter, and display the structural analysis results.

### 1. Setup Subroutines

The subroutines described in this subsection, manipulate the inputs so that the structure may be analyzed. The first subroutine is GEOMETRY, and it is shown in Figure 11. GEOMETRY first calculates the number of elements, $n$. It next determines the global coordinates and incidence angle at each node and calculates the wing area and the chord and thickness lengths at the root and tip. Finally, the subroutine creates a structure array called element for any properties specific to individual elements. The height, width, and incidence angle are calculated for each element.

The next subroutine is called MODIFY_INPUTS. This subroutine assigns the inputs for $E$, $G$, $\rho$, and the box cross section thicknesses to each element. This subroutine exists in case the material properties change for different sections of the

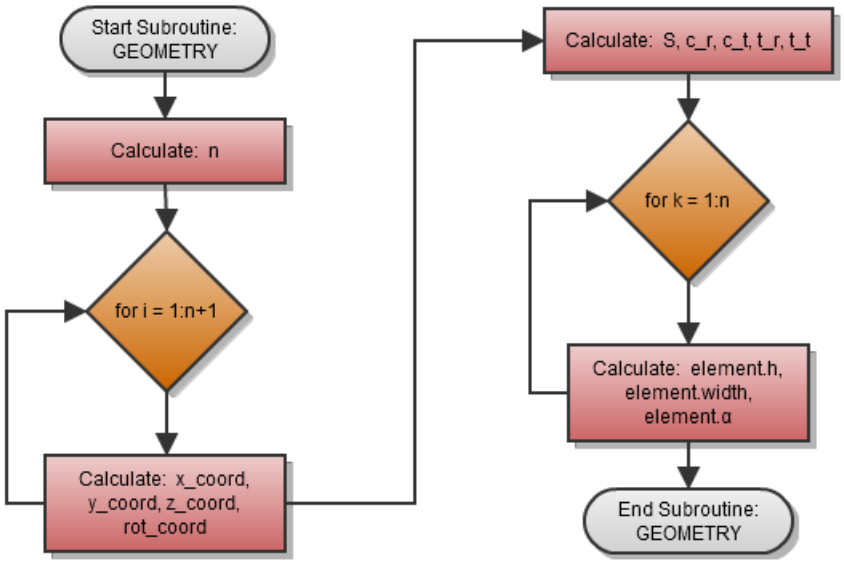


Fig. 11. GEOMETRY Subroutine

wing. The MODIFY_INPUTS subroutine is shown in Figure 12.

The PRINT_VALUES subroutine prints each of the inputs to an output file. Its flow chart has been omitted because it is simple and is not necessary for the functioning of the overall program.

The next subroutine is ELEMENT_VALUES, and it is shown in Figure 13. This subroutine calculates the $A_x$, $J$, $I_{yy}$, and $I_{zz}$ for each element for the rectangular solid or box cross section types. Using the nodal coordinates, the element length, $L$, and direction cosines, $C_x$, $C_y$, $C_z$, are calculated. From the direction cosines, the $\beta$ and $\gamma$ rotation angles are found for each element. This process is described in [27].

### 2. Analysis Subroutines

The next set of subroutines implements many of the equations specified in the previous chapter. These subroutines assemble the stiffness matrix for the structure, impose

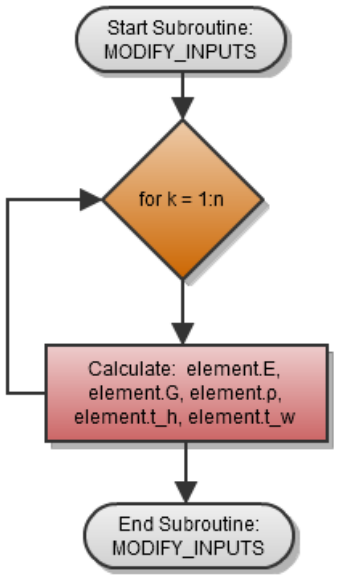


Fig. 12. MODIFY_INPUTS Subroutine

the constraints, assemble the equivalent nodal loads and point loads, then solve the system of equations to determine the nodal displacements.

The first subroutine discussed in this subsection is ASSEMBLE_K. The flow chart for ASSEMBLE_K is shown in Figure 14. First, Equation 2.33 is used and the local elemental stiffness matrices are calculated. Next, the elemental rotation matrices are found using Equations 2.35 - 2.39. Using Equation 2.40, the local elemental stiffness matrices are converted to the global coordinates. Finally, the stiffness matrix for the structure is assembled as described in Equation 2.45. For more details on how this process is implemented, see the subroutine code included in structural tool code which is attached as a supplemental file to this thesis.

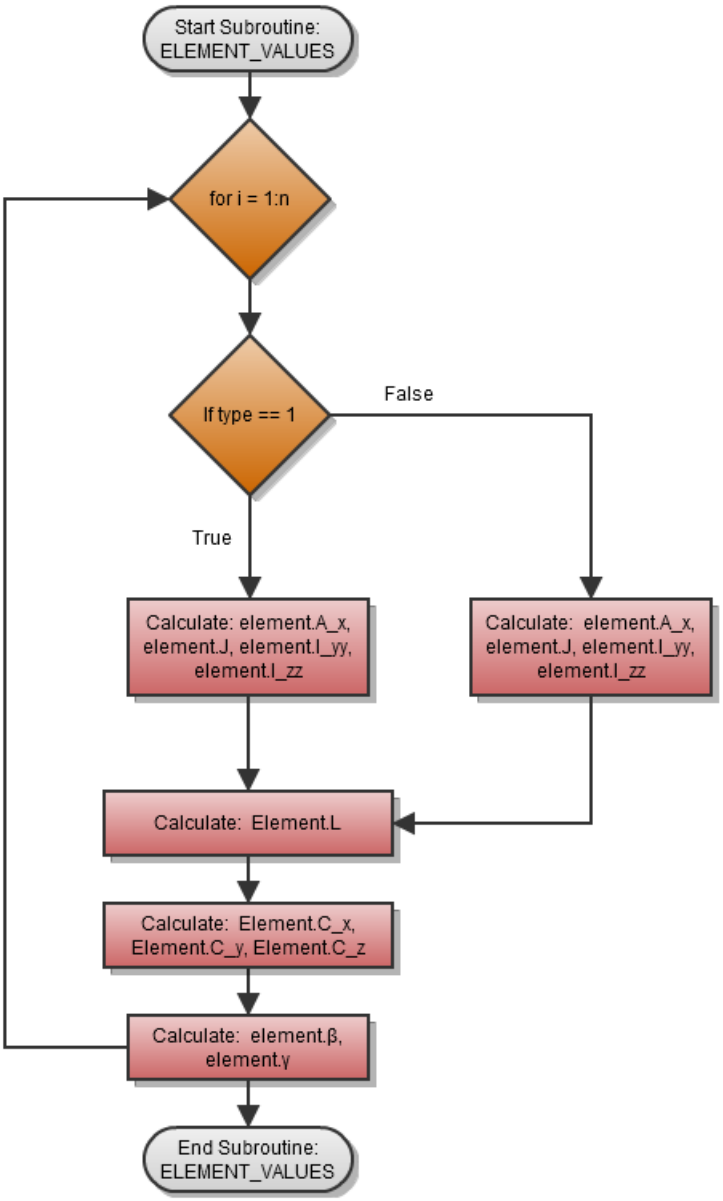


Fig. 13. ELEMENT_VALUES Subroutine

The IMPOSE_CONSTRAINTS subroutine is not shown because it is fairly simple. It adds a value of $10^{30}$ to the indices of the stiffness matrix which correspond to the degrees of freedom constrained by the displacement and rotation boundary

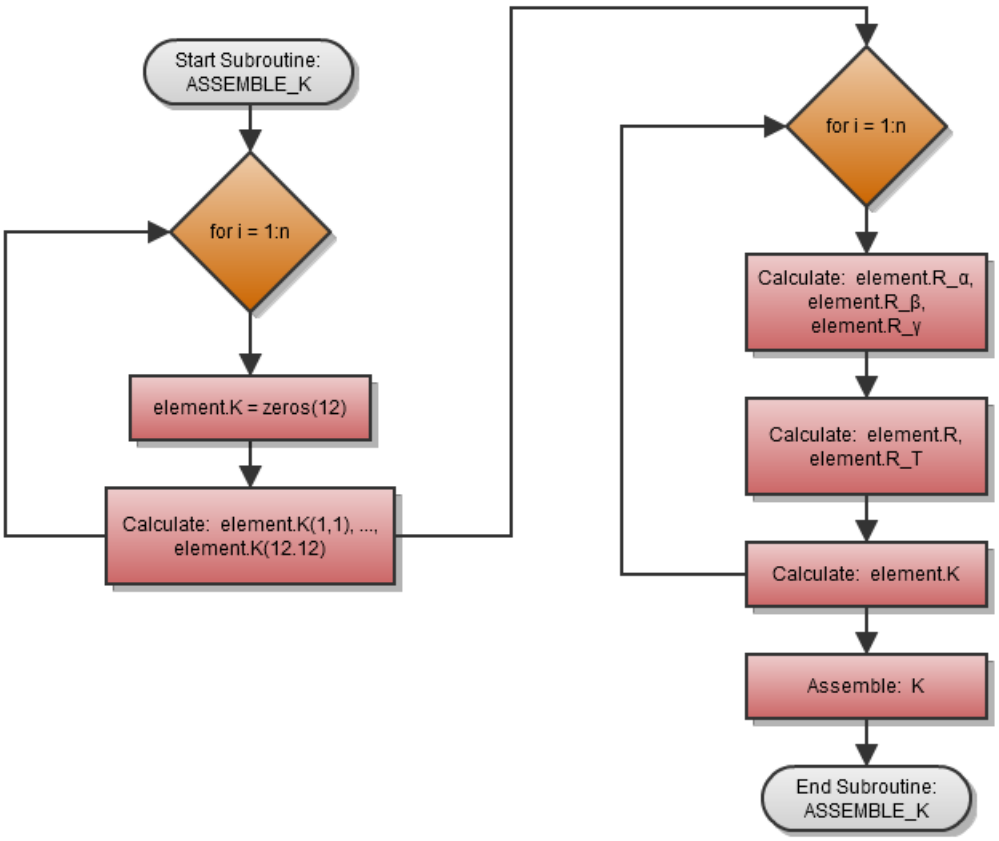


Fig. 14. ASSEMBLE_K Subroutine

conditions.

The next subroutine is ASSEMBLE_Q, and it is shown in Figure 15. As previously mentioned, the aerodynamic loads are input as point loads and need to be converted to loads distributed over the length of each element. First this subroutine uses the units value to determine the gravitational acceleration constant, $g$. Using $g$, $\rho$, and the lift force, the distributed load $f_y$ is calculated for each element. From the drag force and pitching moment, $f_z$ and $m_x$ are calculated for each element. $f_y$, $f_z$, and $m_x$ are then used in Equation 2.34 to determine the equivalent nodal loads

for each element. The equivalent nodal loads for the structure are then assembled following the method described by Equation 2.47.

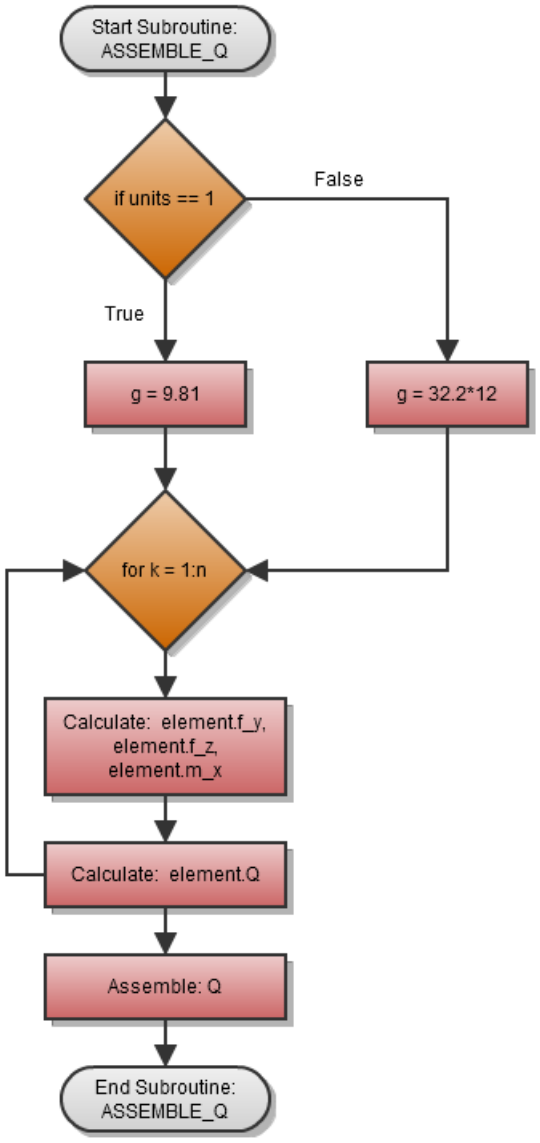


Fig. 15. ASSEMBLE_Q Subroutine

The final two subroutines of the Analysis subsection are the ASSEMBLE_P and SOLVER subroutines. The flow charts for these subroutines are omitted because they are both very simple. ASSEMBLE_P takes the point loads specified at specific nodes in the loads structure array and includes them in the full point load vector **P**. The SOLVER subroutine uses **K**, **Q**, and **P** to solve Equation 2.43 for the nodal displacements **q**.

### 3. Post Processing Subroutines

This subsection describes the subroutines related to the generation of figures showing the displacements, rotations, and axial stress throughout the structure. Most of the flow charts shown in this subsection are very simplified when compared to the actual code. See attached structural tool code for the full details.

The first subroutine is PLOT_DEFLECTION which is shown in Figure 16. The subroutine first finds the individual elemental nodal displacement vectors, $\mathbf{q}_e$, from the full vector **q**. Next, the interpolation functions are found using Equations 2.19 and 2.22. Equation 2.3 uses $\mathbf{q}_e$ and the interpolation functions to calculate the displacements and rotations throughout each element. The elemental rotation matrix must be used to determine the torsional rotations in the local coordinates. Adding the displacements and rotations to the original wing coordinates gives the deflected wing geometry. Finally, the subroutine generates plots of $v$, $y$, $w$, $z$, and $\theta_x$ versus $x$.

The next subroutine is PLOT_DEFLECTION_3D, and it is shown in Figure 17. This subroutine generates a three dimensional wire-frame view of the deflected structure. Because Space Frame FEA only models the deflections of the principal axis, the principal axis is also plotted. The deflections and rotations are very small and will not be observed when the entire structure is shown, so the subroutine uses displacement and rotation scale factors. The displacements and rotations are multiplied

by the scale factors and then used with the element lengths, widths, heights, and axis rotation angles to determine the 3D geometry. The edges of the structure, the connecting lines at the ends of each element, and the principal axis are plotted.

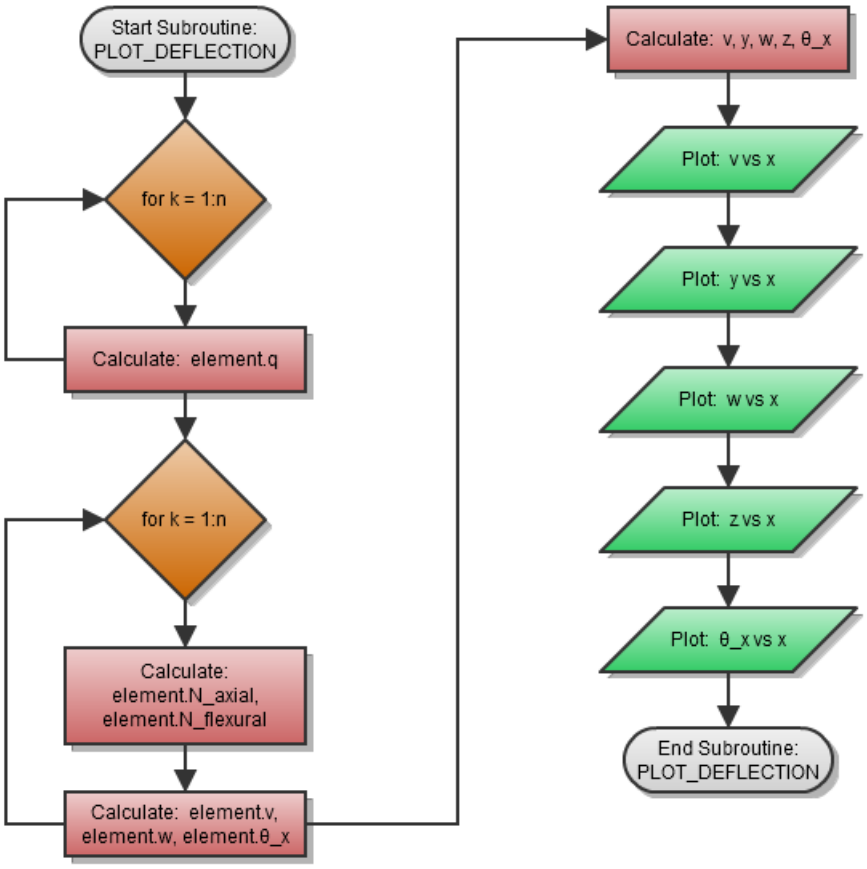


Fig. 16. PLOT_DEFLECTION Subroutine

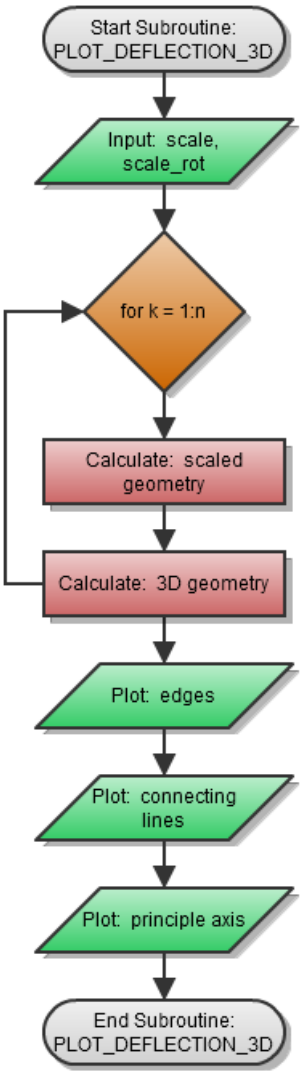


Fig. 17. PLOT_DEFLECTION_3D Subroutine

The STRESS subroutine calculates the axial stress along the principal axis at each node and generates a plot of $\sigma_{xx}$ versus $x$. The flow chart for the STRESS subroutine is shown in Figure 18. In order to calculate the axial stress, $\mathbf{P}_e$ must first be determined by solving Equation 2.14. Next, Equation 2.48 is used to convert $\mathbf{P}_e$ from the global to the local coordinates of each element. Then Equation 2.49 is used

to calculate $\sigma_{xx}$ at each node along the principal axis. At the principal axis, the local $y$ and $z$ coordinates are 0, so the second and third terms of Equation 2.49 are both 0. Finally the subroutine plots $\sigma_{xx}$ versus $x$ for the entire structure.

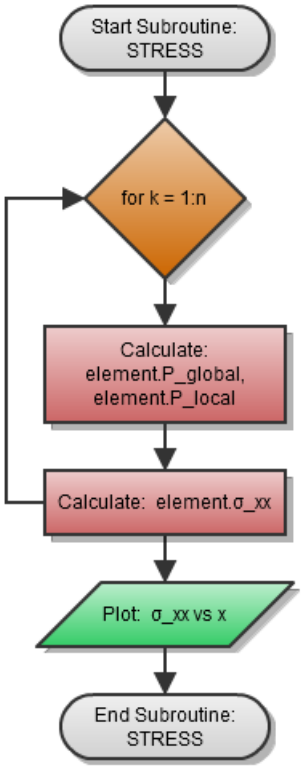


Fig. 18. STRESS Subroutine

The final subroutine, PLOT_STRESS_3D, generates a three dimensional surface plot of the axial stress and is shown in Figure 19. Using Equation 2.49, the axial stress is found at corners of the cross section at incremental spaces within each element. Next, matrices of the global $x$, $y$, and $z$ coordinates and corresponding $\sigma_{xx}$ are found for each of the six surfaces of the rectangular solid represented by the analysis. Surface plots of the axial stress are then made for each of the surfaces.

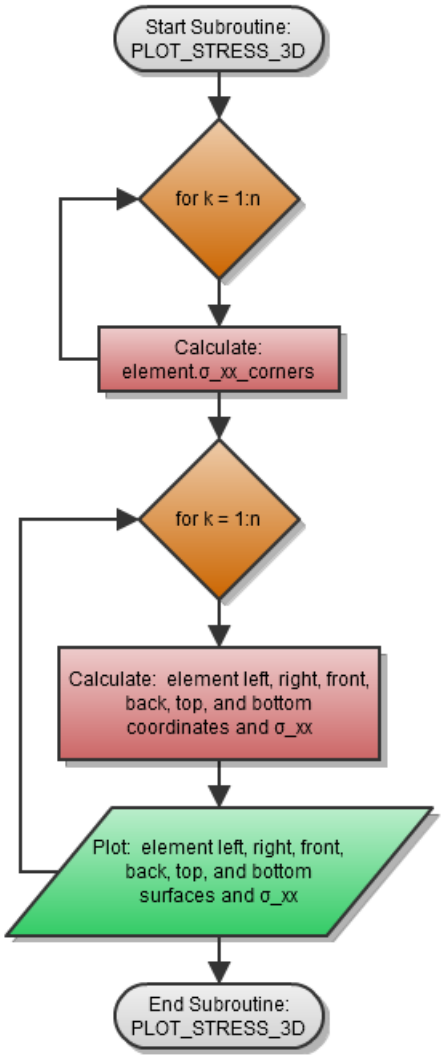


Fig. 19. PLOT_STRESS_3D Subroutine

# CHAPTER IV

# SPACE FRAME FINITE ELEMENT ANALYSIS COMPUTATIONAL TOOL VALIDATION AND VERIFICATION

The purpose of this chapter is to demonstrate that the structural tool is working correctly and may be applied to the morphing wing problem. The first section will validate the tool using the same method of linear beam FEA in Abaqus. The second section will use several more complex FEA models in Abaqus to show that the structural tool is a realistic approach.

## A. Validation

The goal of this section is to demonstrate that the Space Frame FEA structural tool yields physically correct results. The structural analysis program Abaqus is used to generate comparison cases for the Space Frame FEA using the same type of finite element model.

### 1. Case Description

Because the tools developed from this research will primarily be used in development of Micro Air Vehicles and other small scale RC aircraft, similar scale and material properties as the Texas A&M University Manureva RC aircraft wing design project are used for each validation and verification case. More details for the Manureva aircraft are described in Reference [29] and in a later section. The Table I describes the properties used for the validation case. The material properties shown are those of Basswood, which was the material used for the spar caps of the Manureva. Although wood is an orthotropic material, isotropic properties are assumed. A Poisson's ratio

Table I. Validation Case

| Parameter | Value |
|---|---|
| $b\ (in)$ | 80 |
| $AR$ | 10 |
| $\Lambda\ (deg)$ | 0 |
| $\Gamma\ (deg)$ | 0 |
| $c_r$ & $c_t\ (in)$ | 8 |
| $t_r$ & $t_t\ (\%c)$ | 0.12 |
| $\alpha_r$ & $\alpha_t\ (deg)$ | 0 |
| $E_{basswood}\ (psi)$ | $1.537E6$ |

of 0.3 is used for all materials in this chapter.

The structural tool and Abaqus models both contain the right half-span of the wing with a cantilever boundary condition at the wing root. When Abaqus and the structural tool are compared, both models contain the same cross sectional properties. The Abaqus analysis uses the same linear FEA method and Euler-Bernoulli beam model, so the results should match exactly.

Two different cross section cases are evaluated: a solid cross section and a box cross section with 1/8 inch thick walls. The dimensions of the cross sections correspond to the chord length and wing thickness for a wing with zero sweep and zero dihedral. The moments of inertia are described for solid and box cross sections in Equations 2.25, 2.26, 2.27, and 2.28 and the polar moments of inertia are shown in Equations 2.31 and 2.32. For each cross section case, two different load cases are used for the validation: pure lift and pure torsion. The Manureva aircraft had a $3g$ lift load of 22.5 lbs for the half span, so the same load was distributed equally over the

beam model of the wing. The pure torsion case uses a pitching moment of 10 in-lbs applied to the wing tip.

### 2. Solid Cross Section Case

Figure 20 shows the $y$ displacements, $v$, for the case of pure bending due to lift for the solid cross section. As shown in Figure 20, the deflections for Abaqus matched

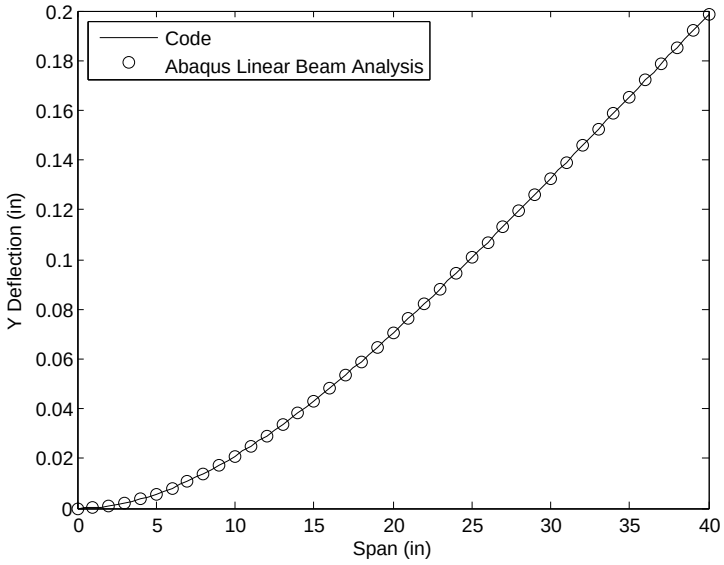


Fig. 20. Linear Euler-Bernoulli Analysis, Deflection due to Lift, Basswood Solid Cross Section

with those generated by the structural tool. The difference between the values is much less than 0.1%, as show in Table II. Figures 21 and 22 show the axial stress for the pure lift load case as generated by Abaqus and the structural tool, respectively. A visual comparison of Figures 21 and 22 shows that the values in the two plots are very close, and an actual numerical comparison of the values at the lower corner nodes of the wing root demonstrates that Abaqus and the structural tool give results within 0.0106%. It should be noted that the three dimensionality of Figure 22 is a

representation of the wing geometry and is not a 3D element model.

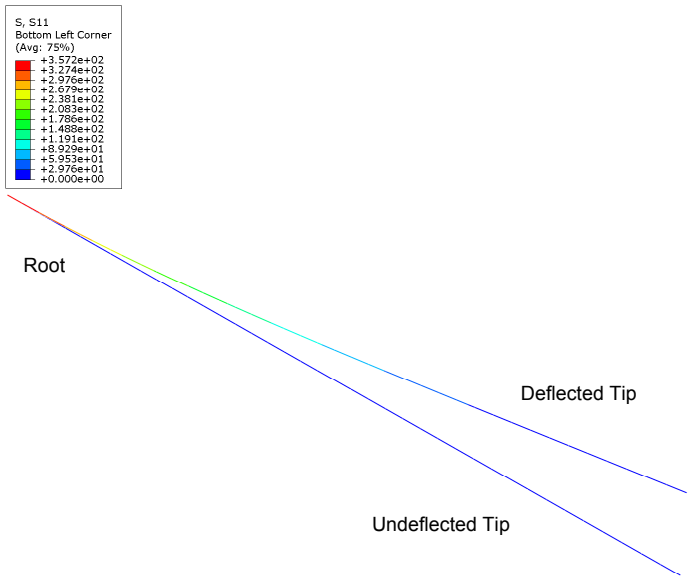


Fig. 21. Linear Euler-Bernoulli Analysis, Abaqus Axial Stress due to Lift, Basswood Solid Cross Section

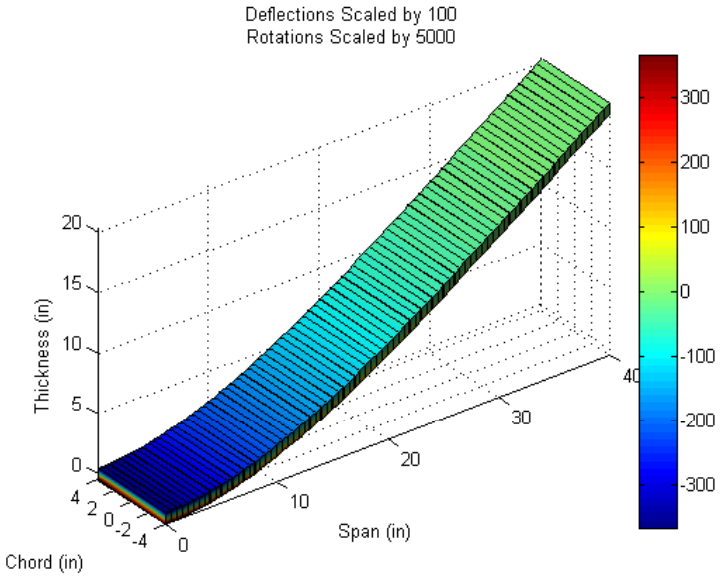


Fig. 22. Linear Euler-Bernoulli Analysis, Structural Tool Axial Stress due to Lift, Basswood Solid Cross Section

Table II. Structural Tool Accuracy Compared to Abaqus Results

| Analysis Type | Beam Type | Material | Cross Section | Deflection Accuracy | Rotation Accuracy |
|---|---|---|---|---|---|
| Linear | Euler-Bernoulli | Basswood | Solid | 5.89E-5% | 0.280% |
| Linear | Euler-Bernoulli | Basswood | Box | 0.942% | 1.11E-5% |
| Linear | Timoshenko | Basswood | Solid | 0.571% | 0.280% |
| Linear | Timoshenko | Basswood | Box | 2.97% | 1.11E-5% |
| Linear | Timoshenko | Balsa | Box | 2.97% | 0.0369% |
| Nonlinear | Timoshenko | Basswood | Solid | 0.569% | 0.280% |
| Nonlinear | Timoshenko | Balsa | Box | 2.59% | 0.0775% |

Figure 23 shows the rotations, $\theta_x$, due to the pitching moment for the pure torsion load case. The comparison shows that the Abaqus and structural tool give results within 0.280% as shown in Table II.

### 3. Box Cross Section Case

This subsection uses the same load cases and wing properties as the analysis described in the previous section, except the cross section is a box with 1/8 inch thick walls. Figure 24 shows the displacements for the pure lift case and Figure 25 shows the rotations for the pure torsion case. Figures 24 and 25 both demonstrate that the structural tool gives very accurate results when compared to Abaqus for the box cross section case. The accuracy for these cases is also shown in Table II.

The validation shows that the structural tool and Abaqus give very similar results for all cross section and load cases. Several other tests were also used to validate the structural tool. By using a symmetric cross section beam, a pure lift case and pure

drag case with equal load values were compared to demonstrate that the deflections due to drag work correctly. The $y$ displacements in the pure lift case were the same as the $z$ displacements in the pure drag case, so it is concluded that the structural tool gives physically correct results. Also, a visual inspection using various geometric input parameters gave the expected output geometry. All results show that the structural tool works correctly and gives accurate results for Space Frame FEA.

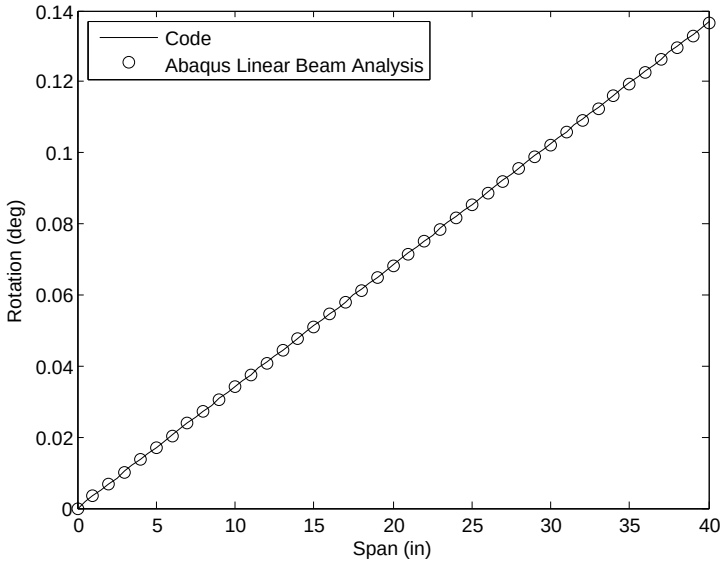


Fig. 23. Linear Euler-Bernoulli Analysis, Rotations due to Pitching Moment, Basswood Solid Cross Section

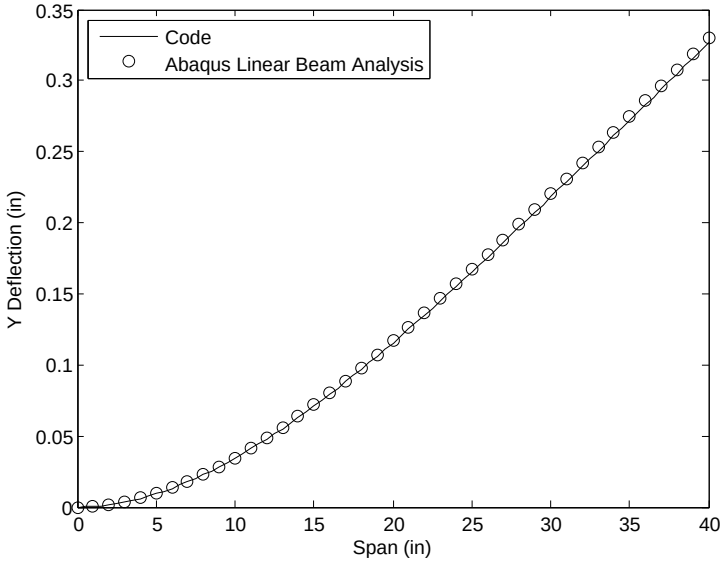


Fig. 24. Linear Euler-Bernoulli Analysis, Deflections due to Lift, Basswood Box Cross Section

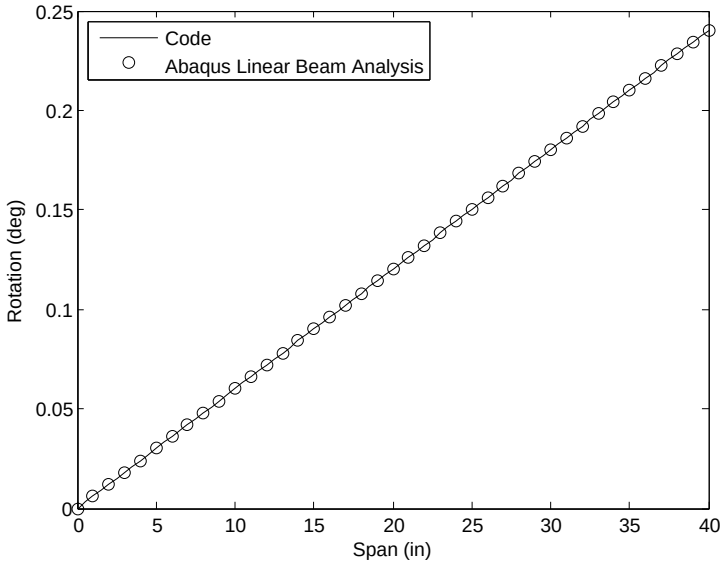


Fig. 25. Linear Euler-Bernoulli Analysis, Rotations due to Pitching Moment, Basswood Box Cross Section

## B. Verification

This section compares the Space Frame FEA structural tool with various types of FEA models generated by Abaqus. Each Abaqus model is more complex and more accurate than the structural tool. The following types of Abaqus models are used in the verification: Timoshenko linear beam model, Timoshenko nonlinear beam model, 3D brick model, and the Manureva wing model. The material and cross sectional properties are the same for the structural tool and Abaqus models for the Timoshenko and 3D brick modesls, but are different for the Manureva wing model. The objective of this section is to demonstrate that the structural tool accurately generates results to a problem with a known solution.

### 1. Timoshenko Linear Beam Model

Timoshenko beam theory is more accurate than Euler-Bernoulli beam theory because it accounts for shear deformations. It is also capable of modeling shorter beams than Euler-Bernoulli beam theory. The structural tool is compared to the Timoshenko model for the geometry parameters described in Table I in the Validation section.

Figure 26 shows displacements for the pure lift case with solid cross section as described in the Validation section. As shown in Figure 26, the structural tool gives results within 0.571% when compared to the Timoshenko beam model for the solid cross section. The pure torsion case also gives very accurate results for the solid cross section as shown in Table II.

The shear deformation effects are slightly more prominent in the box cross section deflection case. Figure 27 shows the displacements due to the pure lift case for the box cross section described in the previous section. The differences between Timoshenko and structural tool deflections are noticeable in Figure 27, but the difference of 0.01

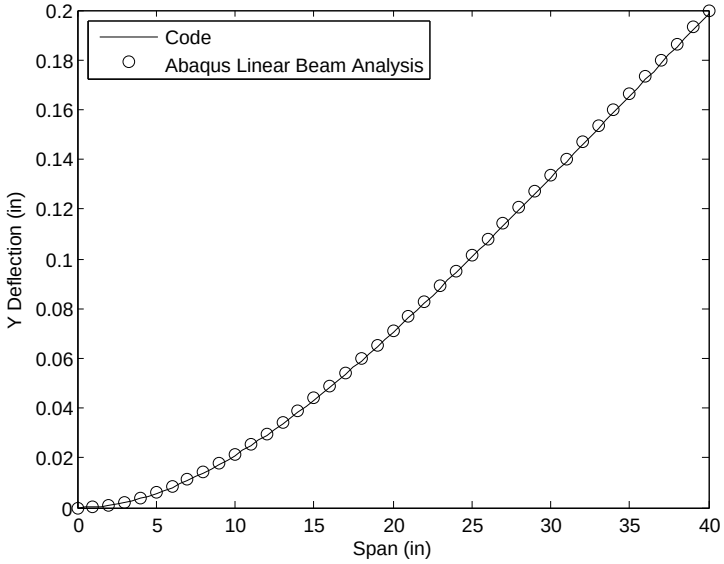


Fig. 26. Linear Timoshenko Analysis, Deflections due to Lift, Basswood Solid Cross Section

inches in the tip deflection is within 2.97% and is very small when compared to the wing half-span of 40 inches. The rotations in the pure torsion case for the box cross section matched closely for the Timoshenko model and the structural tool.

1/8 inch balsa was also used for box cross section with the same load cases. The material properties selected for balsa are an elastic modulus of $1.853E5$ psi and a Poisson's ratio of 0.3. The deflection and rotation accuracy for the balsa case is shown in Table II. The Timoshenko linear beam model shows that the structural tool is very accurate for the given wing geometry.

### 2. Timoshenko Nonlinear Beam Model

Nonlinear analysis uses an iterative method to solve for the deflected wing geometry, and it is more accurate than linear analysis when the deflections become large. For the case described in Table I, Timoshenko nonlinear beam analysis is compared to

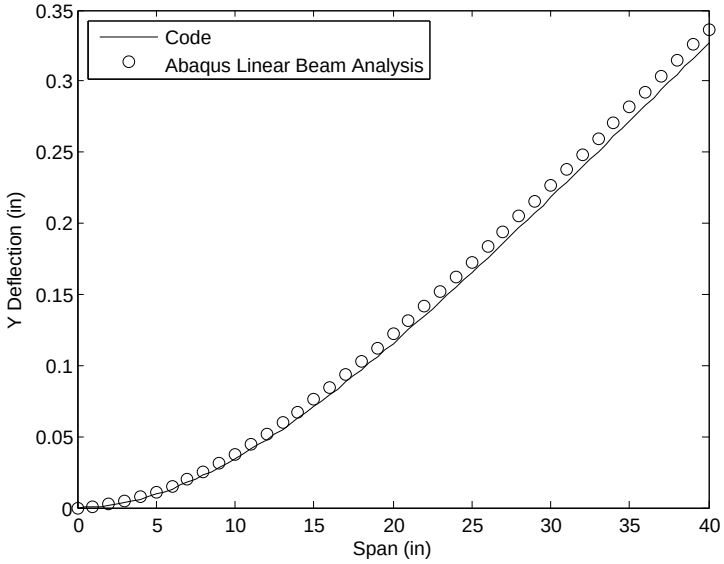


Fig. 27. Linear Timoshenko Analysis, Deflections due to Lift, Basswood Box Cross Section

the structural tool. Figures 28 and 29 show the deflections for the pure lift case and the rotations for the pure torsion case for the solid cross section. As shown in Figures 28 and 29, the structural tool gives results accurate within 0.569% and 0.280%, respectively, when compared to the nonlinear analysis for the basswood solid cross section.

Next, a more flexible structure was modeled in Abaqus using a box cross section with balsa as the material. The results are shown in Figure 30. The accuracy of the structural tool when compared to the nonlinear Timoshenko beam analysis is very close to the accuracy when compared to the linear Timoshenko beam analysis as shown in Table II. The results for the nonlinear beam analysis show that the structural tool is very accurate for the given material properties and loads. If the deflections become much larger due to either loads higher than the $3g$ case or the use of a much more flexible material than basswood or balsa, then nonlinear analysis

may be necessary.

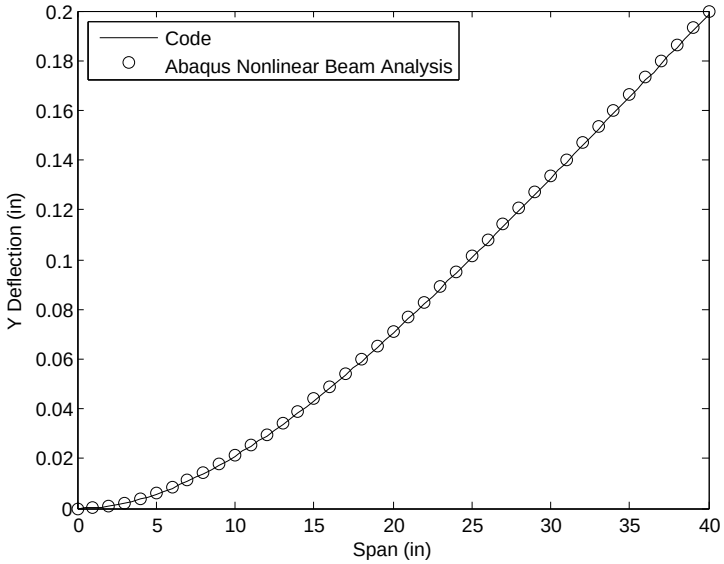


Fig. 28. Nonlinear Timoshenko Analysis, Deflections due to Lift, Basswood Solid Cross Section

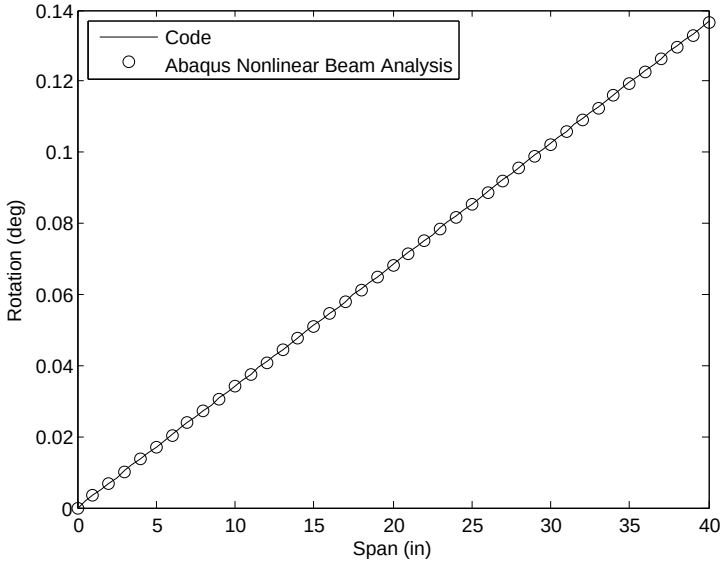


Fig. 29. Nonlinear Timoshenko Analysis, Rotations due to Pitching Moment, Basswood Solid Cross Section

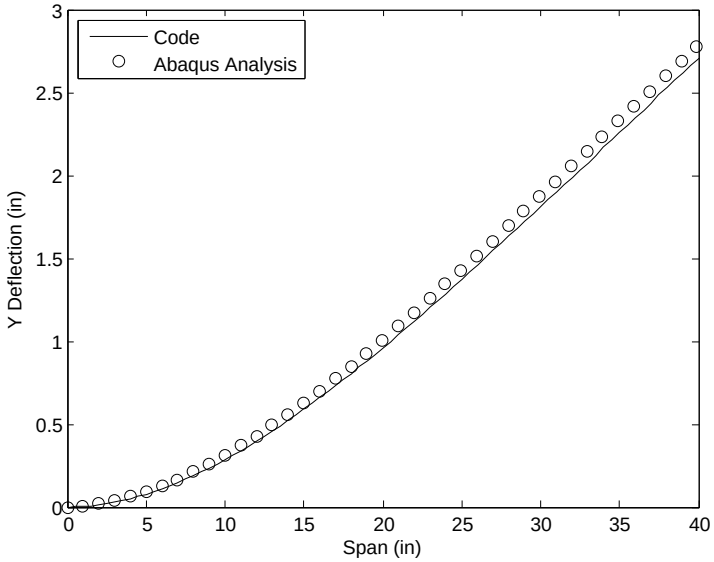


Fig. 30. Nonlinear Timoshenko Analysis, Deflections due to Lift, Balsa Box Cross Section

### 3. 3D Brick Model

The next method of verification uses 3D brick finite elements to model the wing in Abaqus. The objective is to observe the performance of the structural tool for various sweep angles when the load case consists of simultaneous lift and pitching moment loads. An example of the right half-span wing Abaqus model at a 30 degree sweep angle is shown in Figure 31.

The wing structure uses the solid rectangular cross section with the basswood material as described in previous sections. In Abaqus, 60% of the 22.5 lb load is distributed over the area of the forward half of the wing and 40% is distributed over the area of the aft half. The structural tool uses the equivalent lift force and pitching moment distributed over the length of the principal axis. The cases used for comparison consist of sweep angles ranging from 0 degrees to 50 degrees, changing by 10 degree increments. Table III shows the comparison between to structural tool

and Abaqus model wing tip deflections and rotations for each sweep case. It also compares the maximum axial stress at the wing root.

Table III. Structural Tool and Abaqus Model Results for Varying Sweep Angles

| Model | Sweep Angle (deg) | Tip Deflection (in) | Tip Rotation (deg) | Root Maximum Axial Stress (psi) |
|---|---|---|---|---|
| Abaqus | 0 | 0.262 | 0.0623 | 274.4 |
| Structural Tool | 0 | 0.199 | 0.0615 | 366.2 |
| Abaqus | 10 | 0.277 | −0.00630 | 283.0 |
| Structural Tool | 10 | 0.213 | 0.0624 | 382.1 |
| Abaqus | 20 | 0.329 | −0.0959 | 315.7 |
| Structural Tool | 20 | 0.269 | 0.0655 | 438.7 |
| Abaqus | 30 | 0.447 | −0.243 | 380.7 |
| Structural Tool | 30 | 0.404 | 0.0714 | 559.6 |
| Abaqus | 40 | 0.711 | −0.528 | 561.7 |
| Structural Tool | 40 | 0.745 | 0.0812 | 808.4 |
| Abaqus | 50 | 1.40 | −1.18 | 911.9 |
| Structural Tool | 50 | 1.79 | 0.0973 | 1369.9 |

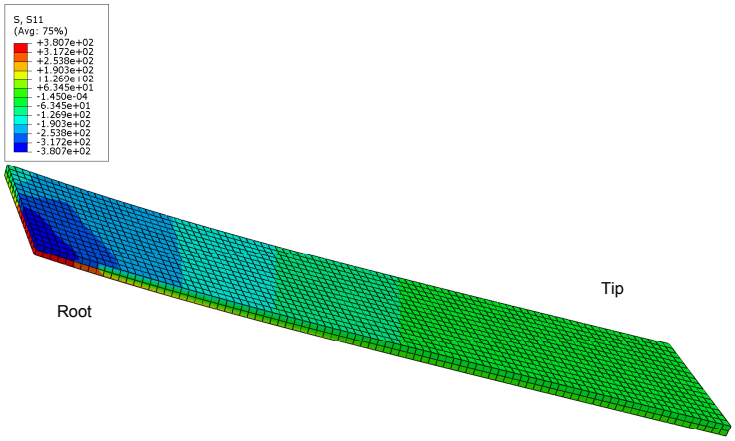


Fig. 31. Abaqus 3D Brick Element Model, 30 Degree Sweep Angle, Axial Stress

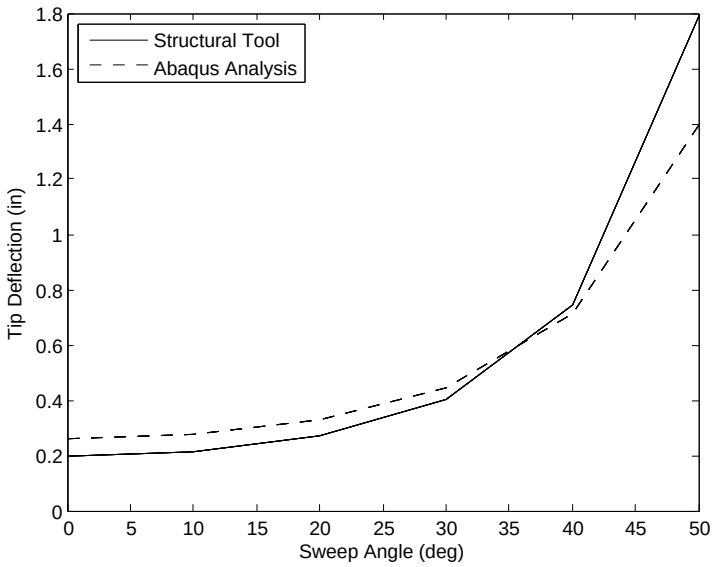


Fig. 32. 3D Brick Element and Structural Tool Comparison for Deflection with Sweep

The values in Table III for tip deflection, tip rotation, and maximum root axial stress are compared to the sweep angle in Figures 32, 33, and 34, respectively. As shown in Figure 32, the structural tool under predicts the tip deflections at the low

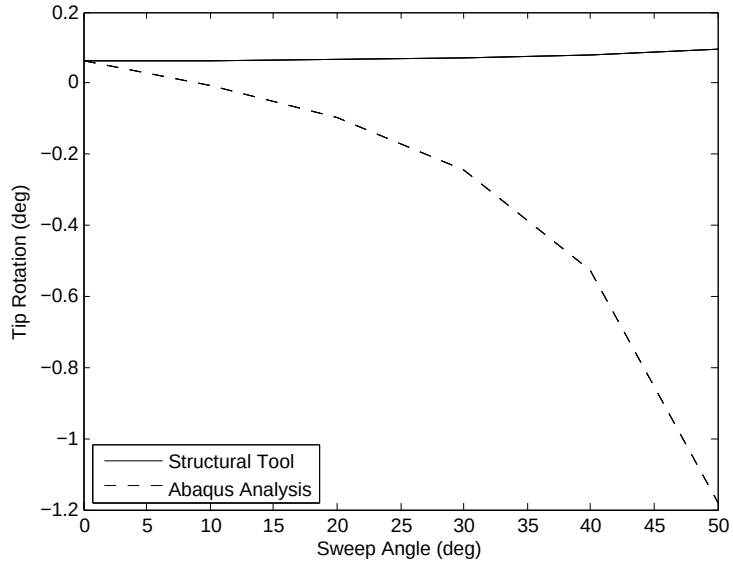


Fig. 33. 3D Brick Element and Structural Tool Comparison for Rotation with Sweep

sweep angles, and it over predicts the tip deflection beginning near 40 degrees sweep.

Figure 33 shows the rotations are very accurate when comparing the two models for the unswept case, but they are very different for the swept cases. The rotation angle is calculated for the Abaqus model using the displacements at the leading and trailing edge wing tip corners. The coupled bending and torsional effects due to sweep and the combined forces and moments create a very complex interaction. A likely reason the rotations are very different in the two models is the elastic axis location in the structural tool model is selected to be on the mid-chord line of the wing. In reality the elastic axis is typically forward of the mid-chord line for a swept wing. Another possible reason the rotations are different is the wing planform shape at the wing tip is different for each of the models. Because the wing planform is modeled as a parallelogram shape in Abaqus, the area near the trailing edge corner of the wing tip is smaller than the area near the leading edge corner for the swept cases. The

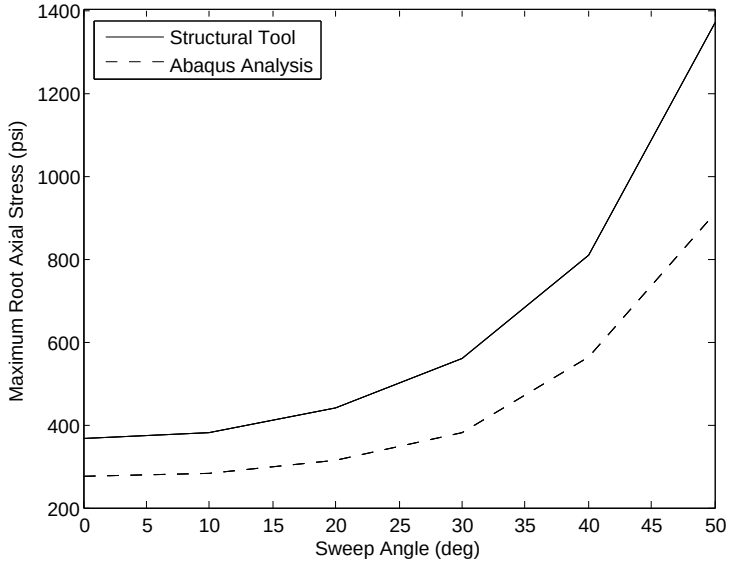


Fig. 34. 3D Brick Element and Structural Tool Comparison for Deflection with Sweep

smaller area near the trailing edge corner may be the reason the trailing edge tip has higher deflections than the leading edge even though aft section loads are smaller. The result is a negative rotation angle for the 3D element model, while the structural tool yields a positive angle for all sweep cases. More investigation of the differences between the 3D element model and beam model is required in order to understand the rotation discrepancy.

When comparing the axial stress in Figure 34, the structural tool over predicts the stress in all sweep angle cases. The major difference between the two models is the cantilever boundary condition at the wing root. For the Abaqus model, the boundary condition is the same for all cases because the shape of the wing planform is a parallelogram. The structural tool models the principal axis for a rectangular wing planform, and the cantilever boundary condition effectively rotates with the wing as it is swept. Because the geometry of the structural tool and Abaqus models are slightly

different, the structural tool does not fully account for the boundary conditions. As shown in Figure 31, the Abaqus models shows higher stress concentrations near the trailing edge root than the leading edge root for the 30 degree sweep case. The structural tool model, shown in Figure 35, shows fairly uniform stress across the wing root.

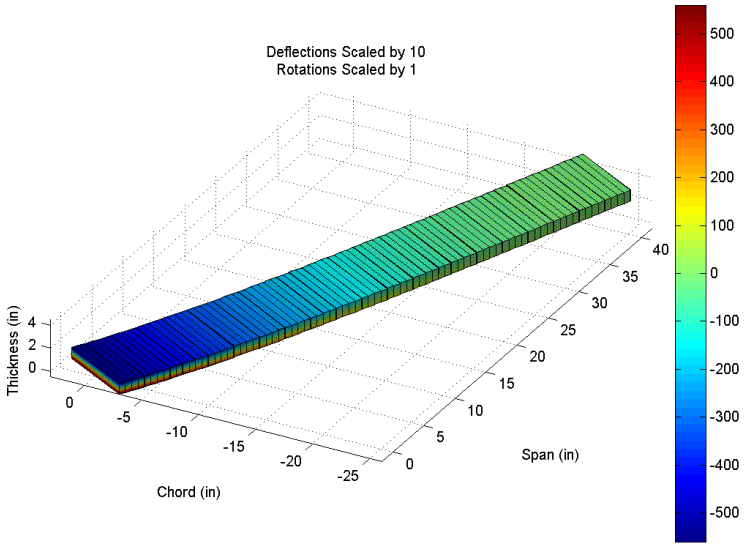


Fig. 35. Structural Tool, 30 Degree Sweep Angle, Axial Stress

Although the structural tool predicts somewhat different results than the Abaqus 3D brick element models, the tool still gives reasonable results in certain cases. In the case of the deflections, the tool predicts results within 0.1 inches from the Abaqus values for all sweep angles less than 50 degrees. This difference in deflections is still extremely small considering the wingspan is 80 inches. The rotation angles were very different for the swept cases, so more investigation of the complex bending and torsion interaction is required to determine the validity of the structural tool. When comparing the axial stresses, the structural tool typically over predicted the stress

by around 100 to 200 psi for the cases less than 50 degrees. This over prediction still gives stress levels which are much less than the maximum allowable stress for basswood. The over prediction of axial stress also makes the structural tool a more conservative estimate. Overall, the 3D brick finite element analysis shows that the structural tool gives somewhat reasonable results for wing sweep angles of 40 degrees or less, but further investigation is still required.

### 4. Manureva Wing Model

The final method of verification uses an Abaqus model for the Manureva wing as described in [29]. An image of the aircraft is shown in Figure 36 and the Abaqus model is shown in Figure 37. The wing model contains the materials, structural

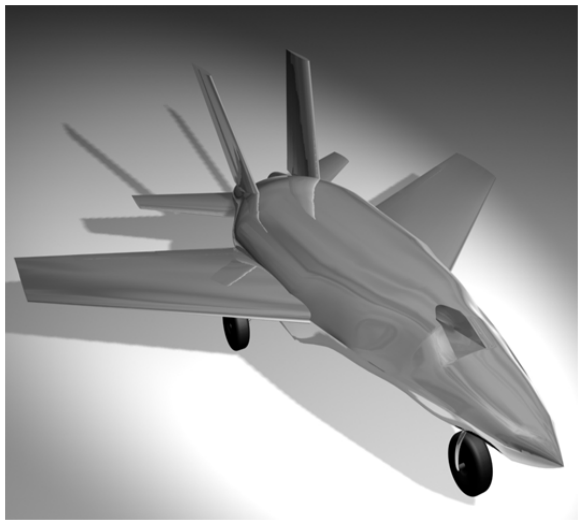

Fig. 36. Manureva Aircraft

components, and finite element types described in Table IV. The Manureva wing in Abaqus models the structure between the forward and aft spars, and all of the loads are applied within this same region. The structural tool also models the region

Table IV. Manureva Abaqus Model Structural Components

| Material | Elastic Modulus (psi) | Thickness (inches) | Structural Component | Element Type |
|---|---|---|---|---|
| Basswood | 1.537E6 | 3/8 | Spar Caps | 3D Brick |
| Balsa | 1.853E5 | 1/8 | Spar Shear Webs | 3D Brick |
| Plywood | 1.8E6 | 1/8 | Ribs, Carry-Through Structure | 3D Brick |
| Monokote | 5.0E4 | 0.01 | Skin | Shell |

between the forward and aft spars, as opposed to the entire wing, in order to accurately approximate the Abaqus model. Table V shows the wing geometric parameters modeled by the structural tool.

The $3g$ lift loads for the half-span Manureva wing are applied in Abaqus, and they are distributed to each of the wing ribs using point loads applied near the forward and aft spars. 65% of the load is applied to the portion of each rib near the forward spar, and 35% is applied to the portion of each rib near rear spar. To represent the equivalent loads in the structural tool, the lift loads are moved to the principal axis and the corresponding pitching moments are applied. Because the loads which are applied near the forward spar give positive moments and those near the aft spar give negative moments, adjacent positive and negative moments are combined. Table VI shows the loads applied in the structural tool.

The Abaqus wing model is more complex than the structural tool. The structural tool uses either a solid rectangular cross section or a rectangular box cross section where as the Abaqus model uses various structural components such as ribs, spar caps, spar shear webs, skin, and a wing carry-through structure. Also, the structural tool

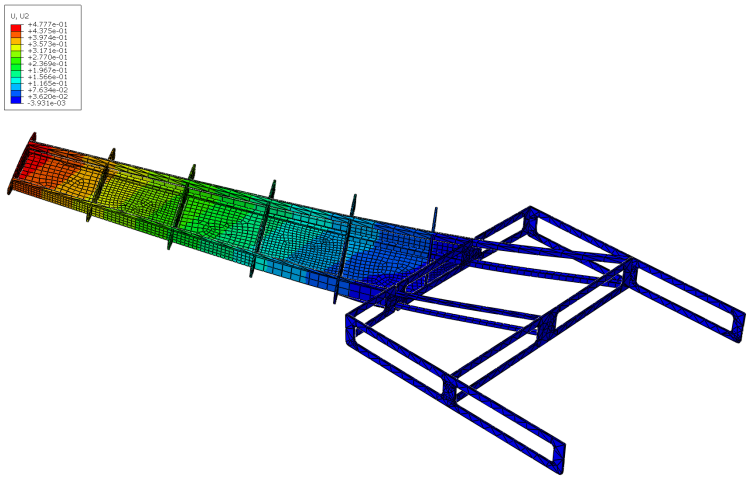

Fig. 37. Manureva Wing Abaqus Deflections

uses only one material and beam finite elements, and the Abaqus model uses various materials and 3D brick elements and shell elements. The boundary conditions for the wing carry-through structure in Abaqus are also more complex than a cantilevered beam. These differences mean that the structural analysis results will be different.

The $y$ displacements throughout the Manureva Abaqus wing model are shown in Figure 37. For the first attempt to model the wing using the structural tool, a box cross section with 1/8 inch basswood was selected. As shown in Figure 38, the basswood is much too stiff. This is to be expected because the Abaqus wing model does not contain nearly as much stiff material as a basswood box cross section. 1/8 inch Balsa was used as the next material and is also shown in Figure 38. The balsa tip deflection is higher than the Abaqus model tip deflection, but the boundary conditions for the Abaqus and structural tool models are also different.

In Abaqus, displacement constraint boundary conditions are applied to the top surface of the forward and aft members of the wing carry-through structure. Figure 39 shows the 1/8 inch balsa structural tool plots with various boundary conditions. One

Table V. Manureva Wing Structure Geometry Parameters

| Parameter | Value |
|---|---|
| $b\ (in)$ | 74.4 |
| $AR$ | 10 |
| $\Lambda\ (deg)$ | 30.8 |
| $\Gamma\ (deg)$ | 0 |
| $c_r\ (in)$ | 9.2 |
| $\lambda_{chord}$ | 0.61 |
| $t_r\ (\%c)$ | 0.27 |
| $\lambda_{thickness}$ | 0.44 |
| $\alpha_r$ & $\alpha_t\ (deg)$ | 0 |

of the plots has the cantilever constraint at 0 inches, and this is the same plot shown in Figure 38. Another structural tool plot shown in Figure 39 has a cantilever boundary condition at the edge of the wing carry-through structure which occurs at 9 inches in the span direction. The 9 inch cantilever location leads to an under approximation of the tip displacement shown in the Abaqus model, so the most realistic location for the cantilever position is somewhere between 0 and 9 inches. Using 3 inches as the location for the boundary condition gives an accurate approximation within 7.10% of the deflections found in Abaqus, as shown in Figure 39.

Comparing the wing tip rotations, the Abaqus model gave rotations of 0.48 degrees where as the structural tool gave 0.16 degrees. The rotations for structural tool are smaller because the balsa along the upper and lower surfaces is more restrictive to the rotations than the monokote skin used in the Abaqus model.

The axial stress within the wing may also be compared between the Abaqus and

Table VI. Structural Tool Manureva Loads

| Lift (lbs) | Span Location (in) | Pitching Moment (in-lbs) | Span Location (in) |
|---|---|---|---|
| 1.46 | 37.2 | 3.6 | 37.2 |
| 0.79 | 34.5 | 5.0 | 33.4 |
| 2.56 | 32.2 | 5.7 | 28.1 |
| 1.38 | 29.0 | 3.5 | 22.8 |
| 3.29 | 27.2 | 2.7 | 17.7 |
| 1.77 | 23.7 | 3.3 | 12.5 |
| 3.29 | 21.8 | | |
| 1.77 | 18.4 | | |
| 2.56 | 17.1 | | |
| 1.38 | 13.0 | | |
| 2.25 | 12.0 | | |

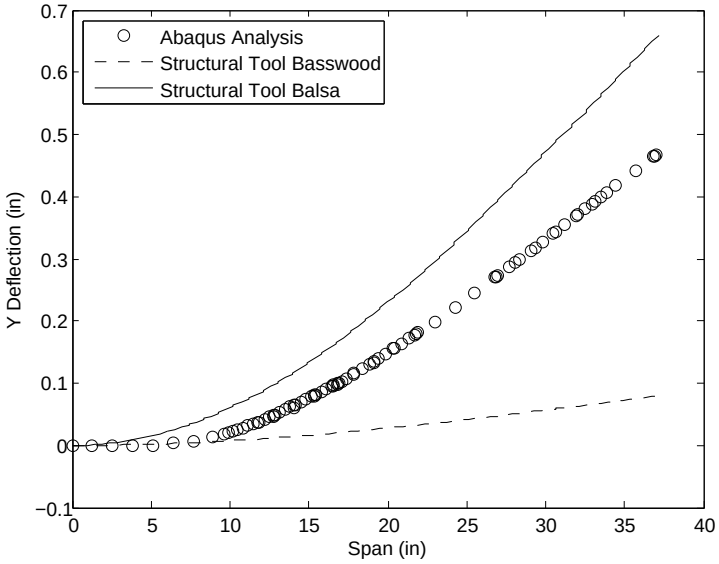


Fig. 38. Manureva Wing Deflections, Material Comparison

structural tool models. Figures 40 and 41 show the axial stress for the Abaqus and structural tool models, respectively. Because the two structures are very different, it is very difficult to compare the axial stresses. The high stress concentrations in the Abaqus model occur in places where the area is very small which are not present in the box structure. In general, the axial stress results found using the structural tool are on the same scale as the Abaqus results for the majority of the wing and give an acceptable approximation.

Modeling the Manureva wing structure using the structural tool does not give a perfect representation of the wing structure, but it gives a reasonable approximation. Overall, the verification shows that the structural tool provides adequate results and is a valid tool for use in future morphing research.

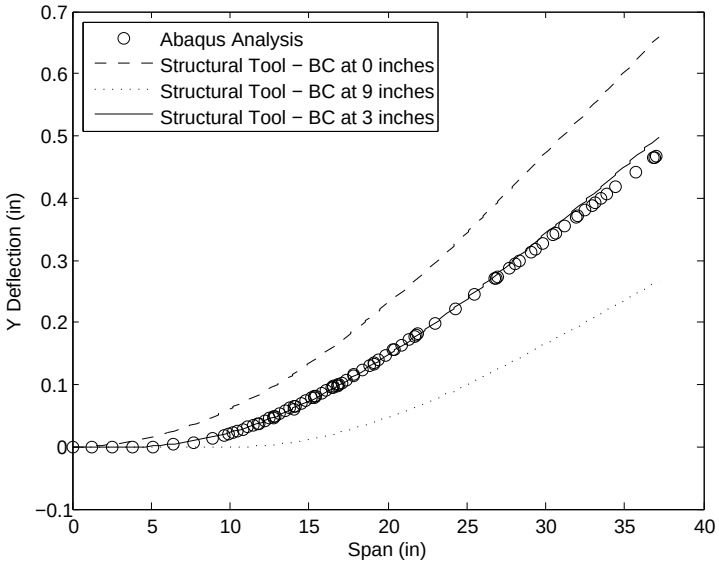


Fig. 39. Manureva Wing Deflections, Boundary Condition Comparison

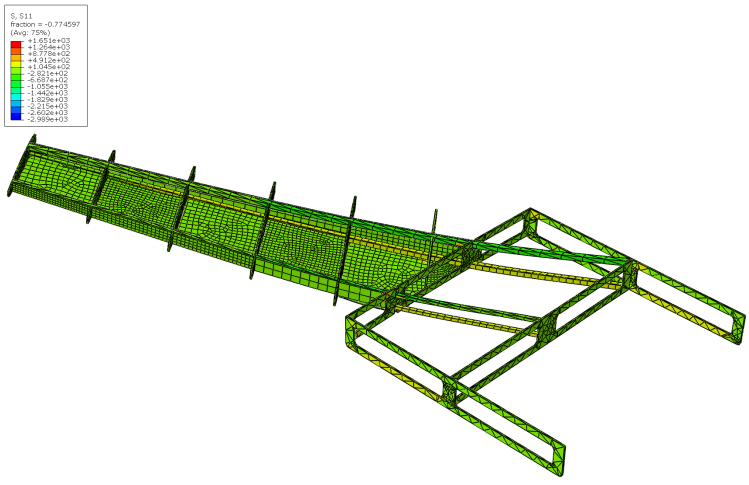

Fig. 40. Manureva Wing Abaqus Axial Stress

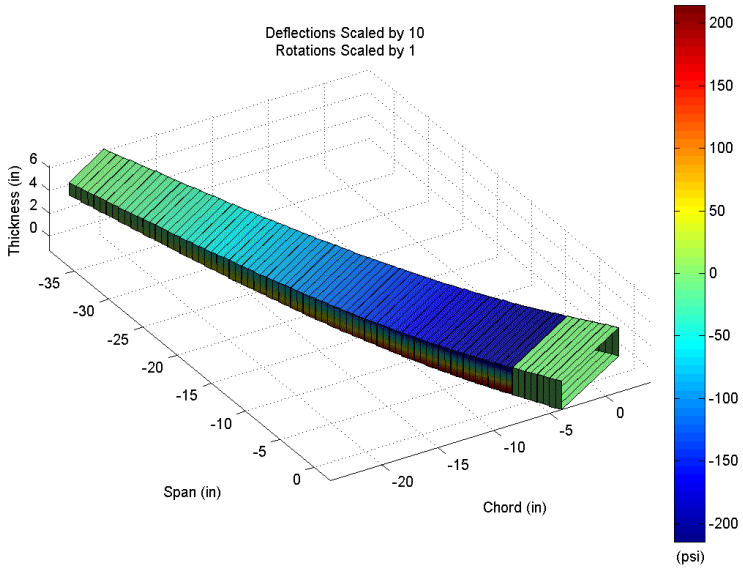


Fig. 41. Manureva Wing Structural Tool Axial Stress

# CHAPTER V

## ITERATIVE QUASI-STATIC AEROELASTIC ANALYSIS

This chapter discusses the interaction between the aerodynamic and structural tools and presents the quasi-static aeroelastic results.

### A. Aerodynamic Tool

This section describes the capabilities and limitations of an aerodynamic tool used for morphing analysis by the Texas A&M University Vehicle Simulation & Control Laboratory. This tool was developed externally to this thesis and is described in in more detail in References [1] and [2]. The aerodynamic tool uses a constant strength doublet-source panel method. The tool assumes that the air flow is incompressible and inviscid, so it is valid for speeds less than Mach 0.3 and while in the linear range of angle-of-attack. It is nominally set to use 130 chordwise panels and 25 spanwise panels for the half-span and is capable of modeling a wing with the morphing parameters described in Chapter I. It models NACA 4-Digit Series airfoil cross sections at the wing root and the left and right wing tips. One limitation of the tool is that it is not programmed to model deflected wing geometries.

The tool uses wing geometry and flight condition inputs and produces the aerodynamic coefficients, $C_L$, $C_D$, and $C_M$, for the wing. $C_L$ is calculated by summing the lift coefficients from every panel. $C_D$ is computed using the parabolic drag polar

$$C_D = C_{D0} + \frac{{C_L}^2}{\pi e AR} \tag{5.1}$$

where the parasite drag coefficient, $C_{D0}$, is found using an approximation based on the wing area, wetted area, and correlation coefficients related to the equivalent skin friction. In Equation 5.1, the second term is known as the induced drag and depends

on the coefficient of lift, and $e$ is the Oswald efficiency factor. The pitching moment coefficient, $C_M$, is calculated by summing the moment coefficient due to the lift coefficient at each panel. The moment arm used to calculate the panel moment coefficients is the longitudinal distance from the panel to the leading edge root. The moment coefficient used in the aerodynamic tool is not adequate for use in the structural tool because the moment is not about the principal axis of the wing.

## B. Integration of Aerodynamic and Structural Tools

This section describes the methods and tool which allow the aerodynamic and structural tools to interact. The MATLAB code used to integrate the tools is called AERO_STRUCTURAL_INTERACTION, and the full code is shown in Appendix B.

### 1. Aerodynamic and Structural Interaction Tool

Two variations of the interaction tool exist. The single pass version calls the aerodynamic and structural tools once, and the iterative version alternates between calling the aerodynamic and structural tools. Flow charts for each version are shown in Figures 42 and 43. The interaction tools each begin with the wing and airfoil geometry inputs and the flight condition inputs. The primary flight condition input is the dynamic pressure of the freestream air flow, $\bar{q}$. Next, the aerodynamic tool is called by the program. An example view of the panel arrangement generated by the aerodynamic tool is shown in Figure 44, where the indices $i$ and $j$ are used to designate the chordwise and spanwise panel locations, respectively.

The interaction tools then modify the outputs of the aerodynamic tool to fit the requirements for the structural tool. The modification process is described in more detail in the subsection below. The structural tool is then called by the interaction

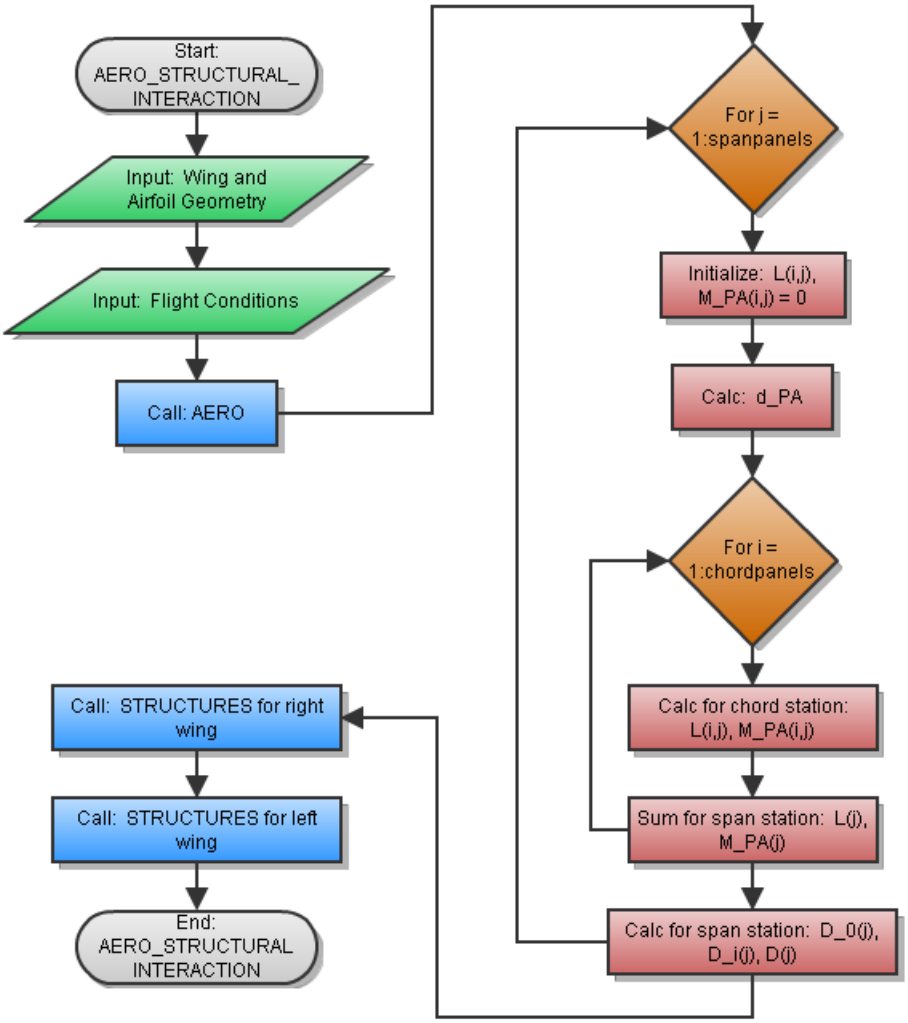


Fig. 42. Non-Iterative Aerodynamic and Structural Interaction Main Program

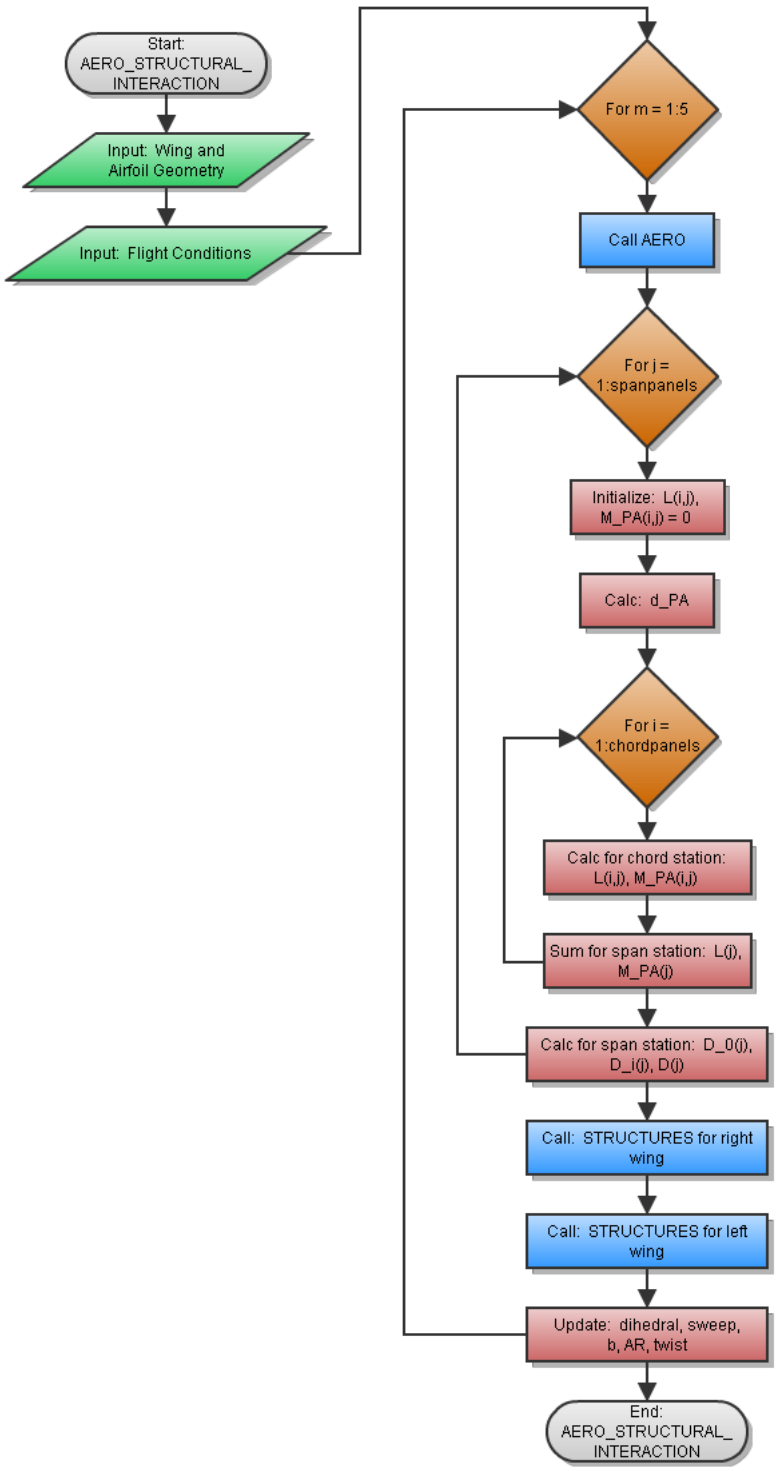


Fig. 43. Iterative Aerodynamic and Structural Interaction Main Program

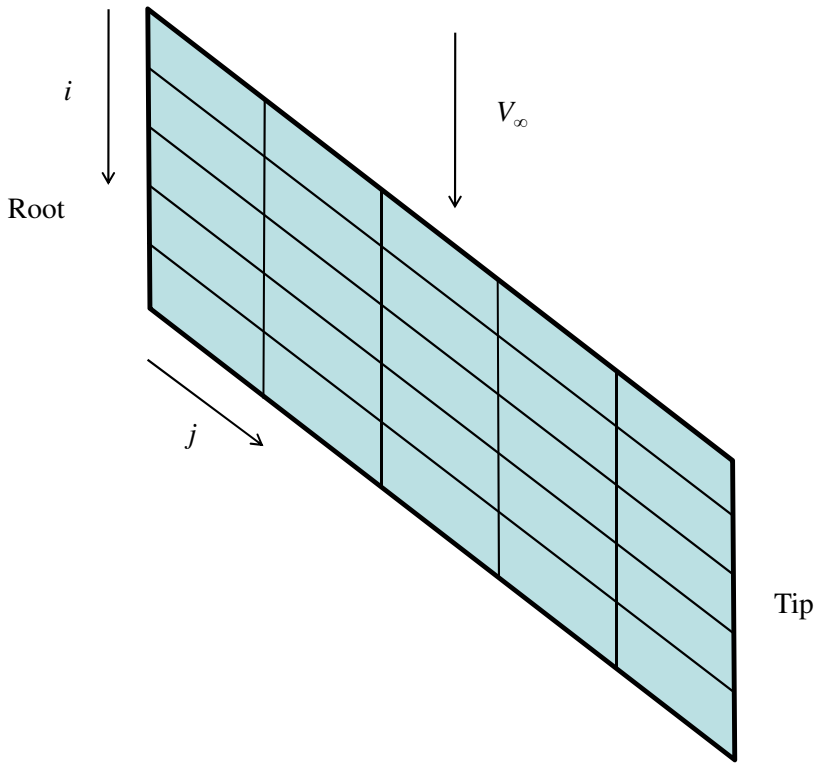


Fig. 44. Panel Arrangement

tool. If the left and right halves of the wing have different geometries, the structural tool must be called twice. For the iterative approach, several geometric parameters are modified by the structural deformations and the aerodynamic tool is called again using the modified geometry. The process repeats until a converged deflected shape is reached. More information regarding the iterative approach and convergence is described in the following subsections.

### 2. Modification of Aerodynamic Loads

The outputs from the aerodynamic tool differ from inputs to the structural tool described in Chapter III, so the aerodynamic outputs must be modified. The spanwise lift, drag, and moments along the principal axis of the wing are needed by the structural tool as opposed to the aerodynamic coefficients. In order to calculate the lift forces needed by the structural tool, the lift coefficients for each panel is converted to force values using the equation

$$L(i,j) = C_L(i,j) \cdot \bar{q} \cdot S \tag{5.2}$$

where the indices $i$ and $j$ correspond to the panel location described in Figure 44. Next, the lift forces at each panel are summed along the chordwise direction which is parallel to the freestream velocity using an equation for the lift force at each span station.

$$L(j) = \sum_i L(i,j) \tag{5.3}$$

The torsional moment, $M_{PA}$, is in the global $x$ direction is about the principal axis. $M_{PA}$ may be found at each panel using the lift force and the distance between the collocation point of the panel, $d_q$, and the principal axis, $d_{PA}$, as shown in the following equation and in Figure 45:

$$M_{PA}(i,j) = -L(i,j) \cdot (d_q - d_{PA}) \tag{5.4}$$

The location of the principal axis may be specified by the user in the code as a percentage of the chord length. The moments are then summed along the chordwise direction. The equation below demonstrates the method to calculate the moments at

each span station.

$$M_{PA}(j) = \sum_{i} M_{PA}(i,j) \tag{5.5}$$

Figure 45 shows the lift and moment locations at each panel before the chordwise panels are summed. The principal axis is shown as a dashed line.

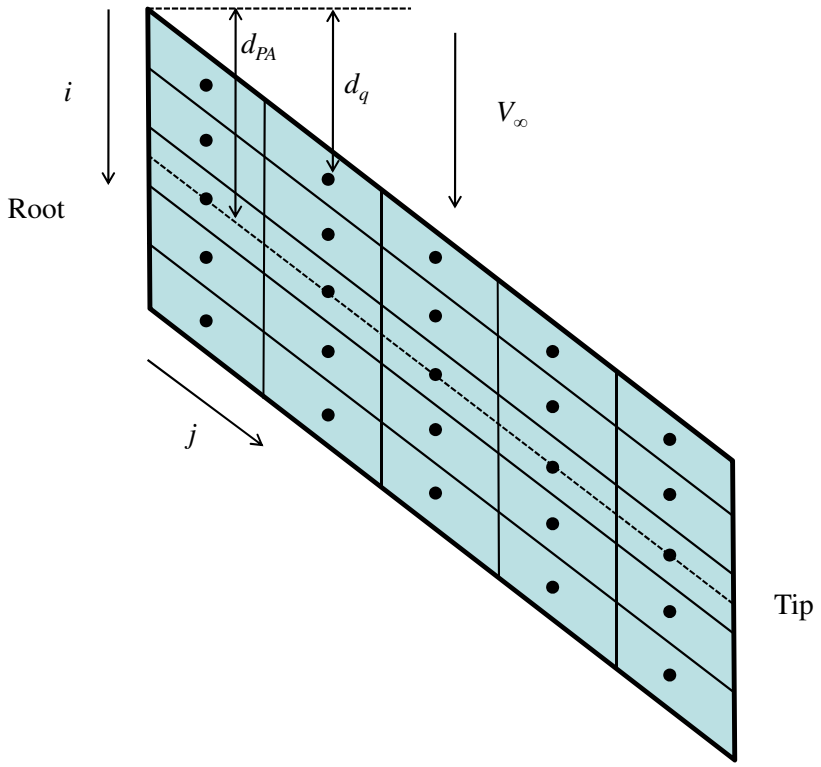


Fig. 45. Panel Lift and Moment Locations

As shown in Equation 5.1, the drag consists of the parasite drag and the induced drag. The parasite drag is approximated by converting $C_{D0}$ into a force by multiplying by the dynamic pressure and wing area. The parasite drag force is then distribed over each span station. Because $C_{D0}$ is a function of the area of the wing, it is distributed over each span station using the ratio of the spanstation area to the total area, as

shown in the following equation.

$$D_0(j) = C_{D0} \cdot \bar{q} \cdot S \cdot \left( \frac{S(j)}{S} \right) \tag{5.6}$$

Because the induced drag is a function of lift, it is approximated by converting $C_{Di}$ into a force using the dynamic pressure and wing area. It is then distributed to each span station in accordance to the ratio of the lift at that span station to the total lift. The following equation demonstrates how the induced drag force at each span station can be approximated.

$$D_i(j) = C_{Di} \cdot \bar{q} \cdot S \cdot \left( \frac{L(j)}{L} \right) \tag{5.7}$$

The total drag at each span station is then found by summing the $D_0$ and the $D_i$ at that location as shown below.

$$D(j) = D_0(j) + D_i(j) \tag{5.8}$$

The methods of calculating $D_0(j)$, $D_i(j)$, and $D(j)$ allow for a distribution of the drag force to each span station which equals the total drag of the wing if every span station is summed.

Figure 46 shows an example of the the locations of the lift, drag, and moments calculated at each span station along the principal axis. These spanwise loads are used as inputs for the structural tool. The methods for calculating the loads at each span station are shown in the AERO_STRUCTURAL_INTERACTION flow charts in Figures 42 and 43.

### 3. Iterative Quasi-Static Aeroelastic Method

After the structural tool is called by the aerodyanmic and structural interaction tool, the wing geometry is deformed. The new geometry has different aerodynamic prop-

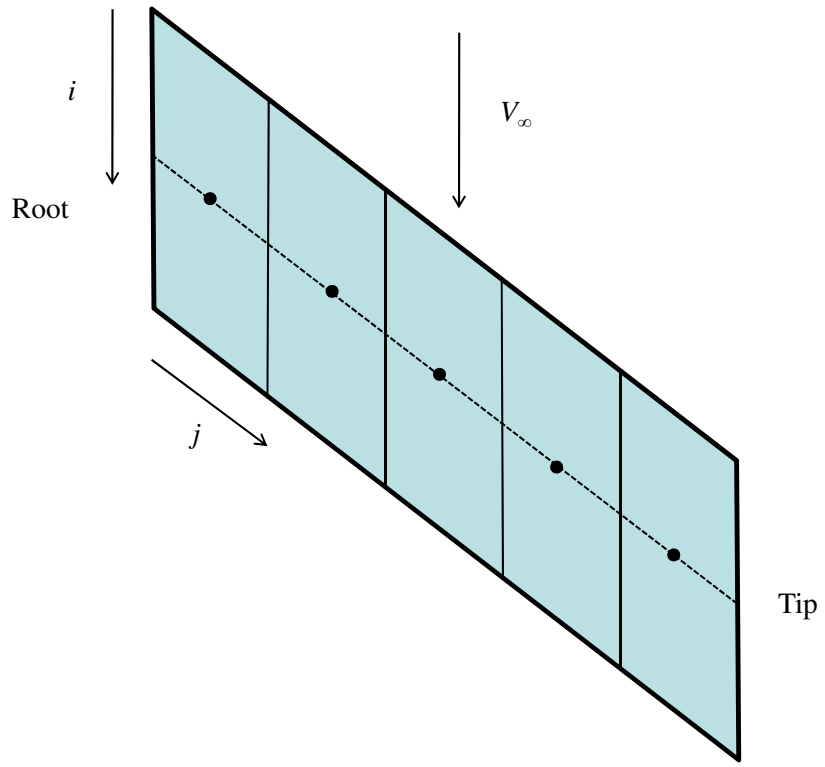


Fig. 46. Lift, Drag, and Moment Locations along Principal Axis

erties, so the new wing configuration must be passed back to the aerodynamic tool as shown in Figure 43.

Various wing parameters must be updated before being passed to the aerodynamic tool. The twist may be updated by adding the rotational deformations due to torsion to the twist angle from the previous iteration. The aerodynamic tool cannot handle a deflected wing shape due to bending, so several other parameters such as the dihedral angle, sweep angle, wing span, and aspect ration must be modified to account for this limitation.

Figure 47 shows an example of the bending displacements, $v$, of a wing due to

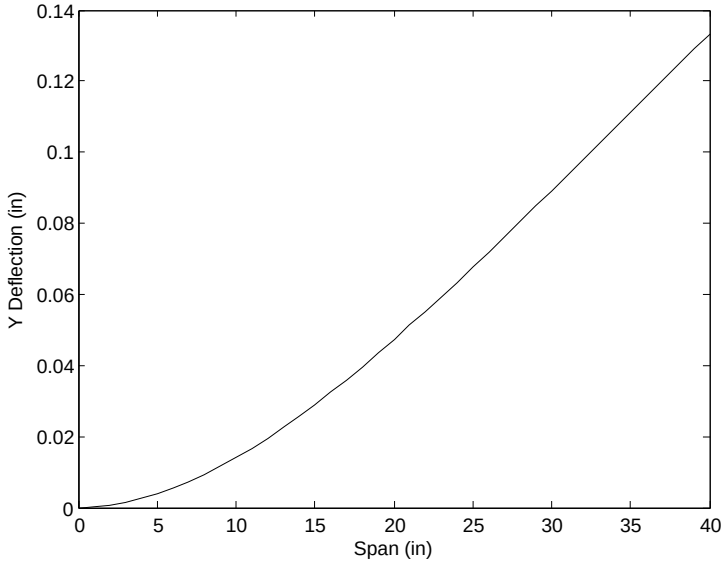


Fig. 47. Wing Displacements due to Lift

lift as calculated by the structural tool. As seen in Figure 47, the displacements are close to linear for the majority of the wing except near the root. Figure 48 compares the deflected wing coordinates with the undeflected shape which has a dihedral angle of 5 degrees. Although the displacements follow a cubic polynomial, most of the curvature occurs near the wing root and rigid body rotations are observed for the majority of the wing span. The result is the deflections follow a straight line for the majority of the wing. Figure 48 shows that the deflected wing shape is similar to the undeflected shape but has a dihedral angle of 5.15 degrees as opposed to 5 degrees. This means that a modified dihedral angle may be passed to the aerodynamic tool to represent the deflected wing shape. A similar event occurs for a wing in bending due to drag, and in this case a modified sweep angle may be passed to the aerodynamic tool. Althought the beam FEA tool does not account for a change in the length of the wing, in reality the deflections cause the wing span to be slightly smaller. The

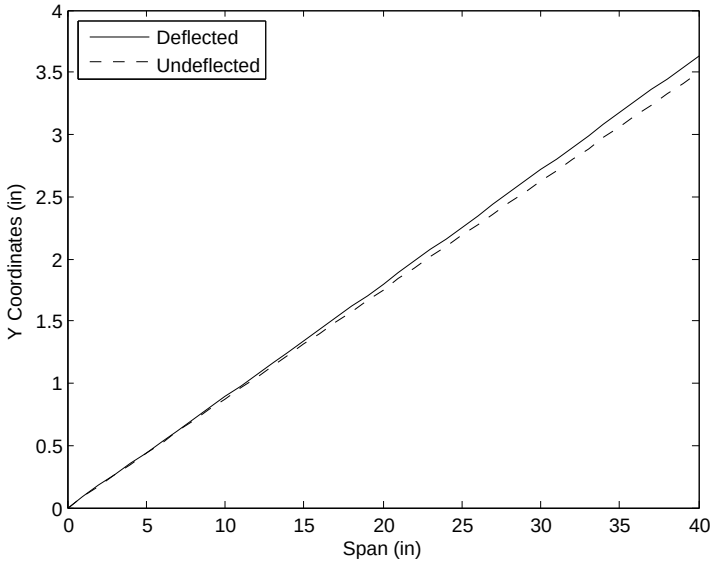


Fig. 48. Deflected and Undeflected Wing Shape

wing span and aspect ratio may be modified to accout for the deflection and passed to the aerodynamic tool. By using the approximate changes to the dihedral angle, sweep angle, wing span, and aspect ratio, the deflected geometry may be passed back to the aerodynamic tool, along with the twist modifications.

## C. Analysis of Aeroelastic Results

The iterative aerodynamic and structural interaction tool calls the aerodynamic tool, calls the structural tool, updates the wing geometry, and then repeats this process in order to determine the aeroelastic effects. The cases considered use the wing geometry and material parameters from the Manureva aircraft detailed in Chapter IV, and a dynamic pressure, $\bar{q}$, of 10 psf is used along with an angle of attack of 4 degrees. The first case iterates using all of the parameters needed to pass back the deflected geometry which include the dihedral angle, sweep angle, wing span, and aspect ratio,

but the twist is not adjusted with each iteration. Table VII shows the wing geometry and aerodynamic coefficients for each iteration. It should be noted that the number of decimal places included in the table are used to show the convergence and do not represent the precision of the aerodynamic and structural tools. As shown, the aerodynamic and geometric properties converge by the second iteration. Figures 49 and 50 show the convergence of the coefficient of lift and the dihedral angle over ten iterations. Figure 51 shows the resulting axial stress for the converged case detailed in Table VII.

Table VII. Geometric and Aerodynamic Iteration Results, No Twist Adjustment

| | Iteration 1 | Iteration 2 | Iteration 3 | Iteration 4 | Iteration 5 |
|---|---|---|---|---|---|
| $\Gamma$ $(deg)$ | 0.257242 | 0.257054 | 0.257054 | 0.257054 | 0.257054 |
| $\Lambda$ $(deg)$ | 30.769966 | 30.769958 | 30.769958 | 30.769958 | 30.769958 |
| $b$ $(in)$ | 74.391546 | 74.391553 | 74.391553 | 74.391553 | 74.391553 |
| $AR$ | 9.997727 | 9.997729 | 9.997729 | 9.997729 | 9.997729 |
| Twist (deg) | 0 | 0 | 0 | 0 | 0 |
| $C_L$ | 0.353889 | 0.353769 | 0.353769 | 0.353769 | 0.353769 |
| $C_D$ | 0.0066400 | 0.0066386 | 0.0066386 | 0.0066386 | 0.0066386 |

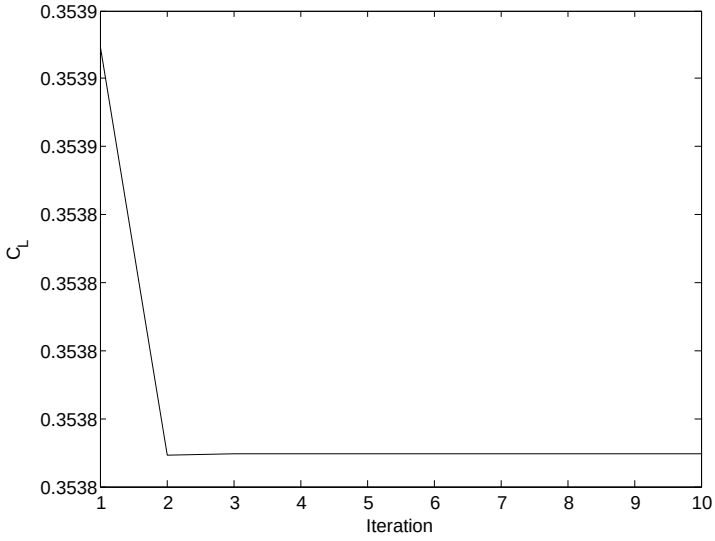


Fig. 49. Converged Coefficient of Lift, No Twist Adjustment Case

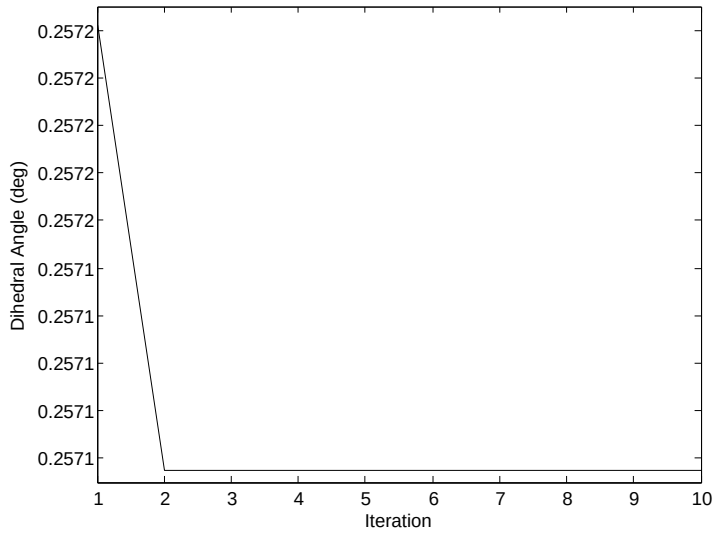


Fig. 50. Converged Dihedral Angle, No Twist Adjustment Case

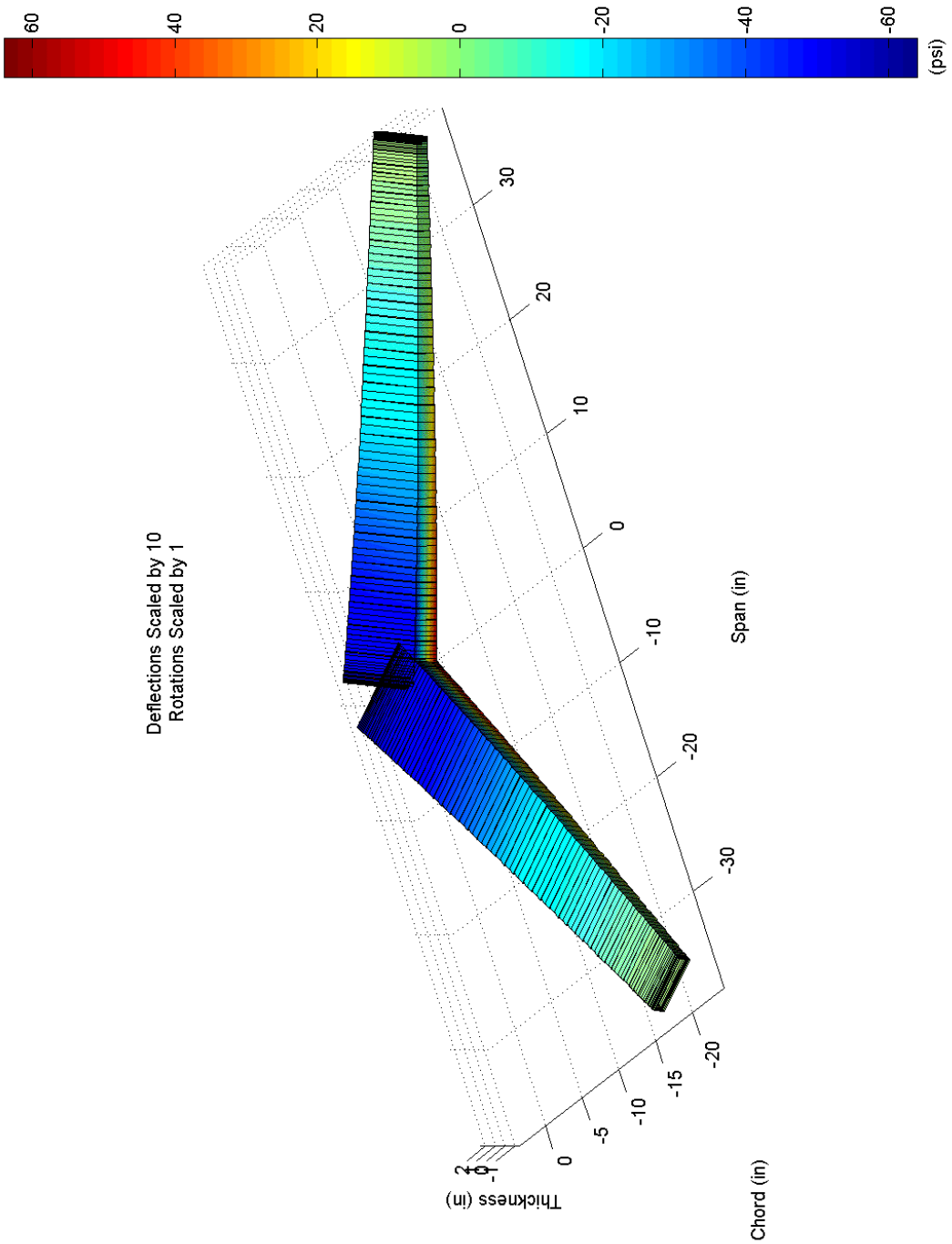


Fig. 51. Axial Stress for Converged Manureva Wing

Table VIII. Geometric and Aerodynamic Iteration Results, Twist Adjustments Included

| | Iteration 1 | Iteration 2 | Iteration 3 | Iteration 4 | Iteration 5 |
|---|---|---|---|---|---|
| $\Gamma$ $(deg)$ | 0.257242 | 0.263478 | 0.270177 | 0.277146 | 0.284397 |
| $\Lambda$ $(deg)$ | 30.769966 | 30.770209 | 30.770471 | 30.770743 | 30.771027 |
| $b$ $(in)$ | 74.391546 | 74.391321 | 74.391078 | 74.390824 | 74.390559 |
| $AR$ | 9.997727 | 9.997667 | 9.997601 | 9.997533 | 9.997462 |
| Twist (deg) | 0.248048 | 0.506790 | 0.775878 | 1.055719 | 1.346732 |
| $C_L$ | 0.353889 | 0.360612 | 0.367754 | 0.375190 | 0.382931 |
| $C_D$ | 0.0066400 | 0.0067415 | 0.0068509 | 0.0069671 | 0.0070906 |

The next case includes the adjustments for twist with each iteration, and the results are shown in Table VIII. As demonstrated by Table VIII, the wing geometric parameters and aerodynamic coefficients continue to increase with each iteration when the twist adjustment is included. Only five iterations are shown in Table VIII, but the trend continues when more iterations are included. Figures 52 and 53 show the trends of the coefficient of lift and the twist angle for 20 iterations. As the twist angle increases, the lift also increases which results in an even higher twist angle the following iteration. The effect is that all of the wing parameters and aerodynamic coefficients continually increase with each iteration, and no convergence is reached.

The iterative results are different for the two cases evaluated in this research. For the case where the twist angle is not adjusted with each iteration, the geometric parameters associated with the wing bending reduced the lift as they increased. The result was a convergence of the wing parameters and aerodynamic coefficients. The case where the twist angle is adjusted with each iteration results in a diverging trend

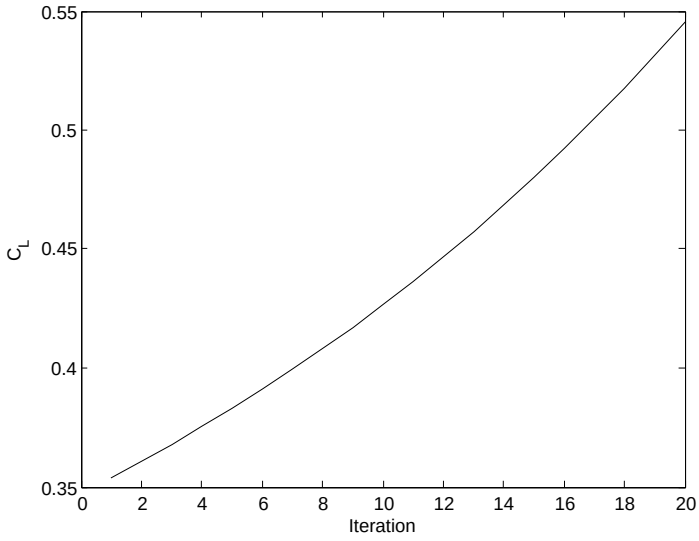


Fig. 52. Coefficient of Lift, Twist Adjustment Case

and no convergence occurs. In reality, a wing aeroelastically deflects to a specific twist angle, as shown in [26]. One potential reason convergence is not reached may be that the problem is not setup correctly in the interaction tool. An additional stiffness term due to the aeroelastic effects may need to be included in addition to the strucutal stiffness matrix which is determined by the structural tool. Because the tool cannot reach a converged solution for the iterative case which includes the twist adjustment, the tool will not be practical for detailed aeroelastic analysis. If a torsionally stiff wing is used for morphing research, the rotational deformations will be small and a single iteration using the interaction tool may provide more than adequate results. Overall, the aerodynamic and structural interaction tool works successfully for one iteration, but future investigation of the convergence case is required in order for the tool to play a key role in future morphing research.

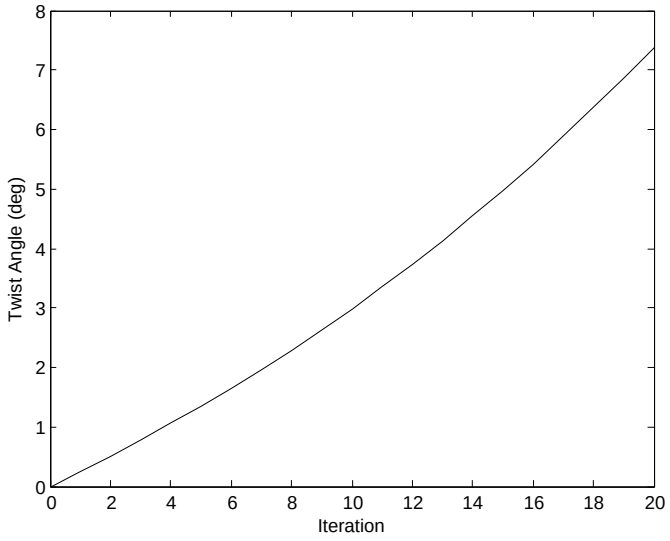


Fig. 53. Twist Angle, Twist Adjustment Case

# CHAPTER VI

## CONCLUSIONS

This thesis describes the development of a structural analysis tool for a reconfigurable wing, and it develops an interaction tool which relates the aerodynamic and structural morphing tools. The structural analysis tool utilizes Space Frame Finite Element Analysis to model an aircraft wing as an Euler-Bernoulli beam with a solid rectangular cross section or a box cross section. The structural tool is capable of modeling a wing with various geometric parameters including wing span, aspect ratio, sweep angle, dihedral angle, chord length, thickness, and incidence angle. By using variable chord length, thickness, and incidence along the span, the tool accounts for wing tapering and twist. Because the tool only models the half-span of the wing, it has the ability to model asymmetric wing shapes by using the tool once for each half-span.

The aerodynamic and structural interaction tool provides the capability to specify the morphing wing geometry, run the aerodynamic tool, and run the structural tool. The loads provided by the aerodynamic tool are used as inputs for the structural tool to obtain a deflected geometry. The tool makes several valid estimates regarding the distribution of wing loading, but it does not change the overall nature of the loads provided by the aerodynamic tool. One version of the interaction tool includes an iterative method which passes the deflected wing geometry back to the aerodynamic tool after running the structural tool. It repeats the process of running the aerodynamic and structural tools for a specified number of iterations. The tools developed in this research may ultimately be used in conjunction with Machine Learning tools to learn the structural and aerodynamic impacts of a wide variety of wing configurations for morphing aircraft.

The following conclusions are made based on the results presented in this thesis:

1. For an implementation using Space Frame FEA theory, the results are validated using linear analysis with Euler-Bernoulli beam properties in Abaqus. The results match within 1% for all cases.

2. By comparing to the more accurate Timoshenko linear beam theory, the structural tool matches within 1% accuracy for the solid cross section, and within 3% accuracy for box cross section. Nonlinear analysis with the Timoshenko beam theory also gave similar results, so the linear analysis used by the structural tool is valid for the material properties and loads which were considered.

3. The 3D brick element Abaqus models show that the structural tool gives somewhat different results than the 3D models, due largely to complex interactions resulting from the coupled bending and torsion effects from wing sweep. The deflections were typically different by less than 0.1 inches, which is very small when compared to the overall wing span. The higher axial stresses predicted by the structural tool make it a more conservative estimate. The verification demonstrates that the structural tool provides somewhat reasonable displacement and stress results for sweep angles up to 40 degrees, but it is significantly less accurate beyond 40 degrees. The structural tool does not predict similar rotational effects for any of the swept cases modeled using 3D brick elements.

4. The structural tool is compared to the Abaqus model for the Manureva RC aircraft wing which contains various materials and complex structural components including spar caps, spar shear webs, ribs, skin, and a wing carry-though structure. Knowing the Abaqus wing results *a priori* make it possible to vary the material properties and boundary conditions of a simplified model which is used in the structural tool. The solution matches within 7% accuracy for the best case studied. The verification using the Manureva model demonstrates

that the structural tool is capable of accurately modeling a complex wing structure, but requires several good estimates of the structural layout and stiffness user inputs.

5. The iterative version of the aerodynamic and structural interaction tool showed that a converged geometry is obtained when the twist angle is not modified during each iteration. For the case when twist is modified, the tool showed divergent behavior in the wing geometric parameters and aerodynamic coefficients. Because these effects should not occur for the case described, the iterative tool is not valid when the twist angle is updated each iteration.

# CHAPTER VII

## RECOMMENDATIONS

1. Since twist is a critical aerodynamic parameter, the convergence issue displayed by the iterative structural interaction tool reduces the utility of the tool for accurate aeroelastic analysis. Further investigation of the aeroelastic convergence issue must be completed to ensure the tool provides realistic results when the twist angle is updated with each iteration. One potential solution is to average each successive rotation angle with the angle calculated by the structural tool during the first iteration. This method is shown to converge, but the convergence values must be validated using aeroelastic theory or data. An iterative method is not required to solve the static rotation problem for a cantilevered swept wing, because an analytical solution to the problem can be obtained. The ratio between the initial twist angle and the rotation calculated using the aerodynamic and structural tools during the first iteration may be used with the analytic solution to determine the final aeroelastically deflected twist angle. This method is demonstrated for a simplified case in Reference [31].

2. Investigate the aspect ratio limitations inherent in the beam elements used by the structural tool. 3D brick element wing models with various aspect ratios ranging from 1 to 9 should be used as comparison cases.

3. Investigate the coupled bending and torsion complex interactions exhibited using the 3D brick element wing models with sweep. The rotations at the wing tip determined by the structural tool showed positive angles while the 3D element model showed negative angles. A better understanding of the interactions is required to determine the validity of the structural tool tip rotations when

sweep is present.

4. Modify the structural tool to utilize Timoshenko beam theory instead of Euler-Bernoulli beam theory. As described in [30], Timoshenko beam theory is capable of modeling beams with a length to thickness ration of 8 to 1, where the thickness is in the direction of loading, while Euler-Bernoulli beam theory is limited to a 15 to 1 ratio. A Timoshenko model is fairly similar and would not require drastic changes to the overall structural tool, but it would allow the ability to model shorter wings.

5. The structural and aerodynamic interaction tool requires an average CPU time of 400 seconds for each iteration, and approximately 98% of the computing time is due to the aerodynamic calculations. An artificial neural network could be developed to model the aerodynamic tool and provide a more computationally efficient alternative. Reference [1] demonstrated the ability of a neural network to reduce the computing time of an airfoil panel method by one order of magnitude.

# REFERENCES

[1] A. Niksch, "Six Degree of Freedom Morphing Aircraft Dynamical Model with Aerodynamics," M.S. Thesis, Texas A&M University, College Station, Texas, August 2009.

[2] A. Niksch, J. Valasek, T. Strganac, and L. Carlson, "Morphing Aircraft Dynamical Model: Longitudinal Shape Changes," in *Proc. of the AIAA Atmospheric Flight Mechanics Conference*, Honolulu, Hawaii, August 2008, number AIAA-2008-6567.

[3] A. Lampton, A. Niksch, and J. Valasek, "Reinforcement Learning of Morphing Airfoils with Aerodynamic and Structural Effects," *Journal of Aerospace Computing, Information, and Communication*, Vol. 6, No. 1, January 2009, pp. 30-50.

[4] A. Lampton, A. Niksch, and J. Valasek, "Morphing Airfoil with Reinforcement Learning of Four Shape Changing Parameters," in *Proc. of the AIAA Guidance, Navigation, and Control Conference*, Honolulu, Hawaii, August 2008, number AIAA-2008-7282.

[5] A. Lampton, A. Niksch, and J. Valasek, "Reinforcement Learning of a Morphing Airfoil-Policy and Discrete Learning Analysis," in *Proc. of the AIAA Guidance, Navigation, and Control Conference*, Honolulu, Hawaii, August 2008, number AIAA-2008-7281.

[6] J. Valasek, M. D. Tandale, and J. Rong, "A Reinforcement Learning - Adaptive Control Architecture for Morphing," *Journal of Aerospace Computing, Information, and Communication*, Vol. 2, No. 5, pp. 174-195, April 2005.

[7] J. Valasek, J. Doebbler, M. D. Tandale, and A. J. Meade, "Improved Adaptive-Reinforcement Learning Control for Morphing Unmanned Air Vehicles," *IEEE Transactions on Systems, Man, and Cybernetics: Part B*, Vol. 38, No. 4, August 2008, pp. 1014-1020.

[8] A. Wickenheiser, E. Garcia, and M. Waszak, "Evaluation of Bio-Inspired Morphing Concepts with Regard to Aircraft Dynamics and Performance," in *Proc. of the SPIE Smart Structures and Materials Conference 2004: Smart Structures and Integrated Systems*, Vol. 5390, 2004, pp. 202-211.

[9] A. Wickenheiser, E. Garcia, and M. Waszak, "Longitudinal Dynamics of a Perching Aircraft Concept," in *Proc. of the SPIE Smart Structures and Materials Conference 2005: Smart Structures and Integrated Systems*, Vol. 5764, 2005, pp. 192-202.

[10] A. Rodriguez, "Morphing Aircraft Technology Survey," in *Proc. of the 45th AIAA Aerospace Sciences Meeting and Exhibit*, Reno, Nevada, January 2007, number AIAA-2007-1258.

[11] M. Motamed and J. Yan, "A Reinforcement Learning Approach to Lift Generation in Flapping MAVs: Simulation Results," in *Proc. of the 2006 IEEE International Conference on Robotics and Automation*, Orlando, Florida, May 2006, pp. 2150-2155.

[12] M. Secanell, A. Suleman, and P. Gamboa, "Design of a Morphing Airfoil Using Aerodynamic Shape Optimization," *AIAA Journal*, Vol. 44, No. 7, pp. 1550-1562, July 2006.

[13] J. Sater, G. Lesieutre, and C. Martin, "A Smarter Transition for Smart Technologies," *Aerospace America*, June, 2006, pp. 18-21.

[14] J. N. Kudva, K. Appa, C. A. Martin, A. P. Jardine, G. Sendeckyj, T. Harris, A. McGowan, and R. Lake, "Design, Fabrication, and Testing of the DARPA/Wright Lab 'Smart Wing' Wind Tunnel Model," Northrop Grumman, Wright Laboratory, NASA Langley, 1997.

[15] J. Bowman, B. Sanders, B. Cannon, J. Kudva, S. Joshi, and T. Weisshaar, "Development of Next Generation Morphing Aircraft Structures," in *Proc. of the 48th AIAA/ASME/ASCE/AHS/ASC Structures, Structural Dynamics, and Materials Conference*, Honolulu, Hawaii, April 2007, number AIAA-2007-1730.

[16] J. Bae, T. M. Seigler, and D. J. Inman, "Aerodynamic and Static Aeroelastic Characteristics of a Variable-Span Morphing Wing," *Journal of Aircraft*, Vol. 42, No. 2, pp. 528-534, March-April 2005.

[17] N. A. Ameri, M. H Lowenberg, M. I. Friswell, and E. Livne, "Modelling Continuously Morphing Aircraft for Flight Control," in *Proc. of the AIAA Guidance, Navigation and Control Conference*, Honolulu, Hawaii, August 2008, number AIAA-2008-6966.

[18] N. Nguyen, "Integrated Flight Dynamic Modeling of Flexible Aircraft with Inertial Force-Propulsion-Aeroelastic Coupling," in *Proc. of the 46th AIAA Aerospace Sciences Meeting and Exhibit*, Reno, Nevada, January 2008, number AIAA-2008-194.

[19] J. Manzo, E. Garcia, A. Wickenheiser, and G. C. Horner, "Design of a Shape-Memory Alloy Actuated Macro-Scale Morphing Aircraft Mechanism," in *Proc. of the SPIE Smart Structures and Materials Conference 2005: Smart Structures and Integrated Systems*, Vol. 5764, 2005, pp. 232-240.

[20] J. Manzo, E. Garcia, A. Wickenheiser, and G. C. Horner, "Adaptive Structural Systems and Compliant Skin Technology of Morphing Aircraft Structures," in *Proc. of the SPIE Smart Structures and Materials Conference 2004: Smart Structures and Integrated Systems*, Vol. 5390, 2004, pp. 225-234.

[21] J. N. Kudva and A. Lockyer, "Exploiting Smart Technologies for Military Aircraft Applications - Perspectives on Development of a Smart Air Vehicle," in *Proc. of the 40th AIAA/ASCE/AHS/ASC Structures, Structural Dynamics, and Materials Conference, AIAA/ASME/AHS Adaptive Structures Forum, AIAA Forum on Non-Deterministic Approaches Conference and Exhibit*, St. Louis, Missouri, April 1999, number AIAA-99-1511.

[22] J. D. Bartley-Cho, D. P. Wang, and J. N. Kudva, "Shape Estimation of Deforming Structures," in *Proc. of the 42nd AIAA/ASME/ASCE/AHS/ASC Structures, Structural Dynamics, and Materials Conference and Exhibit*, Seattle, Washington, April 2001, number AIAA-2001-1566.

[23] J. E. Hubbard Jr., "Dynamic Shape Control of a Morphing Airfoil Using Spatially Distributed Transducers," *AIAA Journal of Guidance, Control, and Dynamics*, Vol. 29, No. 3, pp. 612-616, 2006.

[24] D. H. Allen and W. E. Haisler, *Introduction to Aerospace Structural Analysis*, New York: John Wiley & Sons, 1985.

[25] W. Weaver Jr. and P. R. Johnston, *Finite Elements for Structural Analysis*, Englewood Cliffs, New Jersey: Prentice-Hall, Inc., 1984.

[26] D. H. Hodges and G. A. Pierce, *Introduction to Structural Dynamics and Aeroelasticity*, New York: Cambridge University Press, 2002.

[27] W. Weaver Jr. and J. M. Gere, *Matrix Analysis of Framed Structures: 3rd Edition*, New York: Van Nostrand Reinhold, 1990.

[28] P. F. Pai, *Highly Flexible Structures: Modeling, Computation, and Experimentation*, Reston, Virginia: American Institute for Aeronautics and Astronautics, Inc., 2007.

[29] A. Campbell, B. Eisenbeis, M. Orr, T. Rudloff, and J. York, *Team Manureva: Structural Wing Design Project Final Report*, AERO 405 Course, Professor J. Whitcomb, College Station, Texas A&M University, 2009.

[30] Abaqus, Inc., *Abaqus Analysis User's Manual*, Abaqus Software, Version 6.7, Providence, Rhode Island: Abaqus, Inc., 2007.

[31] J. Wright and J. Cooper, *Introduction to Aircraft Aeroelasticity and Loads*, Chichester, West Sussex, England: John Wiley & Sons Ltd., 2007.

# APPENDIX A

## RESEARCH SCHEDULE

| Task Name | Duration | Start | Finish |
|---|---|---|---|
| **Literature Search** | **70 days** | **Mon 8/25/08** | **Fri 11/28/08** |
| Read Papers | 50 days | Mon 8/25/08 | Fri 10/31/08 |
| Write Summaries | 20 days | Mon 11/3/08 | Fri 11/28/08 |
| **2D FEA Code** | **105 days** | **Mon 9/8/08** | **Fri 1/30/09** |
| FEA Theory Research | 14 days | Mon 9/8/08 | Thu 9/25/08 |
| Main Program and Functions Stiffnesses Matrix, Loads, Solver, and Plot Deflection | 14 days | Fri 9/26/08 | Wed 10/15/08 |
| Function - Plot Deflection 3D | 21 days | Thu 10/16/08 | Thu 11/13/08 |
| Function - Stress | 14 days | Fri 11/14/08 | Wed 12/3/08 |
| Function - Plot Stress 3D | 42 days | Thu 12/4/08 | Fri 1/30/09 |
| **3D FEA Code** | **253 days** | **Mon 1/19/09** | **Wed 1/6/10** |
| Space Frame Theory Research | 21 days | Mon 1/19/09 | Mon 2/16/09 |
| Main Program | 14 days | Tue 2/17/09 | Fri 3/6/09 |
| Function - Geometry | 14 days | Mon 3/9/09 | Thu 3/26/09 |
| Function - Modify Inputs | 7 days | Fri 3/27/09 | Mon 4/6/09 |
| Function - Element Values | 14 days | Tue 4/7/09 | Fri 4/24/09 |
| Functions - Stiffness Matrix and Constraints | 28 days | Mon 4/27/09 | Wed 6/3/09 |
| Functions - Distributed Loads, Point Loads, and Solver | 21 days | Mon 8/24/09 | Mon 9/21/09 |
| Function - Plot Deflection | 14 days | Tue 9/22/09 | Fri 10/9/09 |
| Function - Plot Deflection 3D | 21 days | Mon 10/12/09 | Mon 11/9/09 |
| Function - Stress | 14 days | Tue 11/10/09 | Fri 11/27/09 |
| Function - Plot Stress 3D | 28 days | Mon 11/30/09 | Wed 1/6/10 |
| **Aeroelasticity** | **105 days** | **Mon 11/16/09** | **Fri 4/9/10** |
| Research Aeroelastic Analysis Methods | 21 days | Mon 11/16/09 | Mon 12/14/09 |
| Learn Doublet Panel Code | 14 days | Tue 12/15/09 | Fri 1/1/10 |
| Main Program and Functions CFD and FEA | 14 days | Mon 1/4/10 | Thu 1/21/10 |
| Modify Aerodynamic Loads | 14 days | Fri 1/22/10 | Wed 2/10/10 |
| Iterative Method | 14 days | Thu 2/11/10 | Tue 3/2/10 |
| Results | 28 days | Wed 3/3/10 | Fri 4/9/10 |
| **3D FEA Code Validation and Limitations Using ABAQUS** | **35 days** | **Mon 3/8/10** | **Fri 4/23/10** |
| Linear Beam Theory Cases | 7 days | Mon 3/8/10 | Tue 3/16/10 |
| Nonlinear Beam Theory Cases | 14 days | Wed 3/17/10 | Mon 4/5/10 |
| 3D Element Cases | 14 days | Tue 4/6/10 | Fri 4/23/10 |
| **Thesis** | **154 days** | **Mon 11/16/09** | **Thu 6/17/10** |
| Proposal Writing | 21 days | Mon 11/16/09 | Mon 12/14/09 |
| Proposal Editing | 28 days | Mon 1/25/10 | Wed 3/3/10 |
| Table of Contents and Structure | 7 days | Thu 3/4/10 | Fri 3/12/10 |
| Introduction | 7 days | Mon 3/15/10 | Tue 3/23/10 |
| FEA Theory | 7 days | Wed 3/24/10 | Thu 4/1/10 |
| FEA Code | 7 days | Fri 4/2/10 | Mon 4/12/10 |
| FEA Validation and Limitations | 7 days | Tue 4/13/10 | Wed 4/21/10 |
| Aeroelastic Analysis | 7 days | Thu 4/22/10 | Fri 4/30/10 |
| Editing | 14 days | Mon 5/3/10 | Thu 5/20/10 |
| Defense Charts | 7 days | Fri 5/21/10 | Mon 5/31/10 |
| Defense Presentation | 1 day | Tue 6/1/10 | Tue 6/1/10 |
| Final Editing | 12 days | Wed 6/2/10 | Thu 6/17/10 |

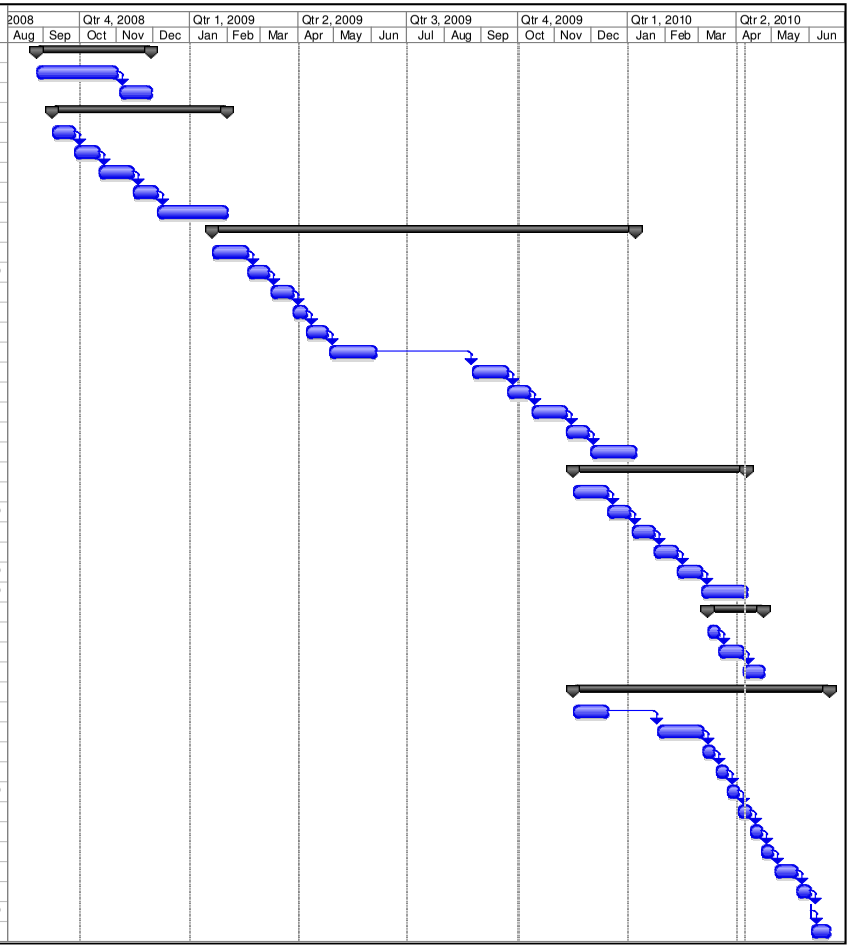


Fig. 54. Research Schedule Gantt Chart

# VITA

Brian Joseph Eisenbeis was raised in Kansas City, MO. He attended Texas A&M University, where he received his Bachelor of Science in Aerospace Engineering (2008) and Master of Science in Aerospace Engineering (2010). He is employed by the Boeing Company in Seattle, WA as part of the Engineering Career Foundation Program.

He may be contacted at the following address:

c/o John Valasek
Texas A&M University
Department of Aerospace Engineering
727D H.R. Bright Building
College Station, TX 77843-3141